

Generalized Least Squares Kernelized Tensor Factorization

Mengying Lei, Lijun Sun*, *Senior Member, IEEE*

Abstract—Completing multidimensional tensor-structured data with missing entries is a fundamental task for many real-world applications involving incomplete or corrupted datasets. For data with spatial or temporal side information, low-rank factorization models with smoothness constraints have demonstrated strong performance. Although effective at capturing global and long-range correlations, these models often struggle to capture short-scale, high-frequency variations in the data. To address this limitation, we propose the *Generalized Least Squares Kernelized Tensor Factorization* (GLSKF) framework for tensor completion. GLSKF integrates smoothness-constrained low-rank factorization with a locally correlated residual process; the resulting additive structure enables effective characterization of both global dependencies and local variations. Specifically, we define the covariance norm to enforce the smoothness of factor matrices in the global low-rank factorization, and use structured covariance/kernel functions to model the local processes. For model estimation, we develop an alternating least squares (ALS) procedure with closed-form solutions for each subproblem. GLSKF utilizes zero-padding and slicing operations based on projection matrices which preserve the Kronecker structure of covariances, facilitating efficient computations through the conjugate gradient (CG) method. The proposed framework is evaluated on four real-world datasets across diverse tasks. Experimental results demonstrate that GLSKF achieves superior performance and scalability, establishing it as a novel solution for multidimensional tensor completion.

Index Terms—Generalized least squares, kernelized tensor factorization, covariance norm, conjugate gradient, multidimensional data completion.

I. INTRODUCTION

MULTIDIMENSIONAL tensors provide a natural representation for real-world data with spatial and temporal structures, such as traffic state measurements (e.g., speed or flow), color images, digital videos, functional MRI scans, and user-item rating records. With the rapid development of data acquisition technologies, such datasets are increasingly prevalent and play a vital role in numerous applications. However, a critical challenge in analyzing tensor-structured data is the ubiquitous problem of sparsity and incompleteness. As a result, tensor data recovery has emerged as a central research problem in areas including traffic state imputation [1]–[3], image/video inpainting [4], signal processing [5], and remote sensing [6].

The key to tensor completion lies in leveraging the relationships between observed and missing entries. Given the intrinsic low-dimensional structure of real-world multidimensional

data, low-rank modeling approaches—such as matrix/tensor factorization (MF/TF) with a pre-specified rank [7], nuclear-norm minimization-based matrix/tensor completion (MC/TC) [8], and advanced tensor decompositions like tensor ring and tensor train decomposition [9]—have been widely studied. A major limitation of standard low-rank factorization models is their permutation invariance along each dimension, which prevents them from incorporating additional constraints or side information on the latent factors. Consequently, these models often overlook local smoothness—critical structural prior information such as spatial correlations among neighboring sensors or temporal continuity in traffic measurements.

To overcome this issue, smoothness constraints or regularizations are frequently integrated into low-rank frameworks. Examples include total variation (TV) and quadratic variation (QV)-regularized tensor decompositions [10], graph-constrained matrix [11] and tensor learning [12]–[14], and autoregressive modeling regularized methods for both matrix [15] and tensor completion [1], [16]. While these smoothness-constrained models effectively capture global, low-frequency structures, they often fail to account for high-frequency, locally varying dependencies. In practice, the residuals of such approximations exhibit local correlations that reflect rapid variations—for example, sudden drops in traffic speed due to incidents or sharp edges in digital images. Capturing these local variations within a single low-rank model may require a substantial increase in rank, leading to prohibitive computational costs [10]. Addressing this limitation demands frameworks that can jointly capture both global and local structures in a computationally efficient manner.

In this paper, we propose the **Generalized Least Squares Kernelized Tensor Factorization** (GLSKF) framework for recovering incomplete multidimensional tensors. GLSKF additively integrates two complementary components: (1) a low-rank, covariance-constrained/smoothed tensor factorization, $\mathcal{M} = \sum_{r=1}^R \mathbf{u}_1^r \circ \mathbf{u}_2^r \circ \dots \circ \mathbf{u}_D^r$, which models the global structure of the data, and (2) a correlated residual module, \mathcal{R} , that captures local dependencies. The overall data model is expressed as $\mathcal{Y} \approx \mathcal{M} + \mathcal{R}$. This additive structure was initially introduced in [17] for Bayesian uncertainty quantification via computationally intensive Markov chain Monte Carlo (MCMC) methods. In contrast, GLSKF adopts a deterministic framework with scalable optimization techniques, enabling efficient point estimation for tensor completion. To enforce smoothness, we define a *covariance norm*—equivalent to assuming Gaussian process (GP) priors on the latent factors and residuals—and design structured covariances for the latent factors along with a product kernel having banded sparse co-

Mengying Lei and Lijun Sun are with the Department of Civil Engineering, McGill University, Montreal, Quebec, H3A 0C3, Canada. E-mail: mengying.lei@mcgill.ca (Mengying Lei), lijun.sun@mcgill.ca (Lijun Sun).

* Corresponding author.

variance matrices for the residuals. Exploiting the properties of Kronecker products and sparse computations, our approach allows for scalable solutions. The resulting optimization problem is solved via alternating least squares (ALS) with closed-form updates. For missing data, projection matrices that preserve the Kronecker covariance structure enable efficient matrix–vector multiplications using the conjugate gradient (CG) method. The computational cost scales linearly with the data size, i.e., $\mathcal{O}(J_{CG}RN)$, where $N = \prod_{d=1}^D I_d$ and J_{CG} is the number of CG iterations, making GLSKF highly efficient and suitable for large-scale applications. Moreover, the incorporation of a local residual component reduces the required rank for the global factorization, further enhancing efficiency.

The main contributions of this work are summarized as follows:

- (i) **Additive Framework for Global and Local Correlations:** We integrate a global covariance-constrained low-rank factorization component with a locally correlated residual process in an additive model, thereby capturing both long-range, low-frequency structures and short-scale, high-frequency variations. We introduce a generalized *covariance norm* derived from covariance matrices; minimizing this norm enforces smoothness in both the latent factors and the local process.
- (ii) **Scalable Solution Algorithms:** We develop efficient ALS algorithms with closed-form updates for model estimation. Projection matrices for missing indices are employed to preserve the Kronecker structure of the covariances. By leveraging Kronecker matrix–vector multiplications and sparse matrix computations via the CG algorithm, the computational cost is significantly reduced, ensuring scalability for large-scale multidimensional datasets.
- (iii) **Comprehensive Evaluation:** We conduct extensive experiments on various real-world multidimensional datasets for missing data completion. The results demonstrate that the proposed GLSKF framework achieves superior performance and computational efficiency compared to existing low-rank methods.

The remainder of this paper is organized as follows. Section II surveys related work on kernelized tensor modeling and additive frameworks. Section III introduces notation and background on constrained factorization models. Section IV describes the GLSKF methodology, including its global-local additive structure and scalable optimization algorithms. Section V presents experimental results on four real-world tensor completion tasks. Section VI analyzes model scalability and the impact of key components, and Section VII concludes the paper with a summary of contributions and directions for future research.

II. RELATED WORK

The proposed GLSKF framework models correlations in the latent space by constraining the smoothness of latent factors using a covariance norm—a quadratic regularization derived from positive semidefinite (PSD) covariance matrices. This norm, central to the “kernelized” aspect of GLSKF, is equivalent to assuming Gaussian process (GP) priors on the latent

factors in probabilistic frameworks. Prior work has explored kernelized low-rank modeling for spatiotemporal data, including probabilistic approaches [2], [18], [19] and optimization-based methods. For example, [20] introduced covariance-based quadratic norms for principal component analysis (PCA) and matrix decomposition to encode structured correlations, while [21] applied kernel-weighted norms to tensor decomposition.

The covariance-based smoothness constraint in GLSKF serves as a flexible and generalized regularization framework. Many commonly studied constraints can be reinterpreted as specific instances of covariance constraints with equivalent kernel or covariance functions [22]. For instance, as noted in [2], temporal state-space dynamics [16] and autoregressive regularizations [15] correspond to covariance norms based on the Ornstein-Uhlenbeck (OU) process and Matérn class covariance matrices, respectively. Similarly, graph-based constraints [11] are equivalent to covariance norms using a graph Laplacian kernel. In Section IV, we demonstrate the equivalence between quadratic variation (QV) smoothness constraints and covariance norms by setting the covariance constraint matrix \mathbf{K} as $(\mathbf{K})^{-1} = \mathbf{L}^\top \mathbf{L}$, where \mathbf{L} represents the differentiation or smoothness constraint matrix, as defined in [10].

A key innovation of GLSKF lies in its additive integration of complementary components: a global low-rank kernelized factorization and a locally correlated residual module. The idea of separately modeling global and local correlations through distinct components has been studied in various contexts. For example, in probabilistic spatial modeling, [23], [24] combined reduced-rank covariance approximations with tapered, compactly supported covariances to capture long-range and short-scale dependencies in large spatial datasets. Similarly, in functional data analysis, [25], [26] augmented matrix completion with banded covariances for process estimation. However, these approaches often incur high computational costs for multidimensional data with missing entries, as missing data disrupt the Kronecker structure of covariance matrices.

More recently, additive low-rank models have been combined with plug-and-play (PnP) modules incorporating neural networks to encode local priors [27]. While effective, these neural network-based components often lack the interpretability and simplicity provided by covariance-based modeling. In contrast, GLSKF employs a generalized least squares (GLS) loss to model correlated residuals within a kernel-smoothed low-rank framework. A related approach using GLS to impose correlations on model errors was proposed in [20]. However, their method integrates out the local component, applying constraints solely to the global low-rank space and thus failing to handle missing data effectively.

The most closely related work to GLSKF is the Bayesian complementary kernelized model (BCKL) [17], designed for Bayesian inference in multidimensional spatiotemporal data. While both GLSKF and BCKL utilize an additive structure, their primary objectives differ: GLSKF focuses on scalable estimation, whereas BCKL emphasizes uncertainty quantification. BCKL depends on computationally intensive MCMC methods, often requiring thousands of iterations to approximate the posterior distributions of factor parameters and GP hyperparameters. In contrast, GLSKF leverages efficient

iterative optimization with carefully designed procedures tailored to each variable, achieving deterministic point estimates. This approach significantly reduces computational costs while ensuring high accuracy.

III. PRELIMINARIES

A. Notations

Throughout this paper, lowercase letters denote scalars (e.g., x), boldface lowercase letters denote vectors (e.g., $\mathbf{x} \in \mathbb{R}^M$), and boldface uppercase letters denote matrices (e.g., $\mathbf{X} \in \mathbb{R}^{M \times N}$). The ℓ_1 and ℓ_2 norms of a vector \mathbf{x} are defined as $\|\mathbf{x}\|_1 = \sum_m |x_m|$ and $\|\mathbf{x}\|_2 = \sqrt{\sum_m x_m^2}$, respectively. For a matrix $\mathbf{X} \in \mathbb{R}^{M \times N}$, its (m, n) th entry is denoted by either x_{mn} or $\mathbf{X}(m, n)$. We denote the $N \times N$ identity matrix by \mathbf{I}_N .

Given two matrices $\mathbf{A} \in \mathbb{R}^{M \times N}$ and $\mathbf{B} \in \mathbb{R}^{P \times Q}$, the *Kronecker product* is defined as

$$\mathbf{A} \otimes \mathbf{B} = \begin{bmatrix} a_{1,1}\mathbf{B} & \cdots & a_{1,N}\mathbf{B} \\ \vdots & \ddots & \vdots \\ a_{M,1}\mathbf{B} & \cdots & a_{M,N}\mathbf{B} \end{bmatrix} \in \mathbb{R}^{MP \times NQ}.$$

The *Hadamard product* (i.e., element-wise product) for two matrices \mathbf{A} and \mathbf{B} of the same dimensions is denoted by $\mathbf{A} \circledast \mathbf{B}$, and the *outer product* of two vectors \mathbf{a} and \mathbf{b} is denoted by $\mathbf{a} \circ \mathbf{b}$. If $\mathbf{A} = [\mathbf{a}_1, \dots, \mathbf{a}_N]$ and $\mathbf{B} = [\mathbf{b}_1, \dots, \mathbf{b}_N]$ have the same number of columns, the *Khatri-Rao product* is defined as the column-wise Kronecker product: $\mathbf{A} \circledast \mathbf{B} = [\mathbf{a}_1 \otimes \mathbf{b}_1, \dots, \mathbf{a}_N \otimes \mathbf{b}_N] \in \mathbb{R}^{MP \times N}$. The *vectorization* of a matrix \mathbf{X} , denoted by $\text{vec}(\mathbf{X})$, stacks all its columns into a single vector.

Following the tensor notation in [28], a third-order tensor is denoted by $\mathcal{X} \in \mathbb{R}^{M \times N \times P}$, and its mode- k unfolding (with $k = 1, 2, 3$) is denoted by $\mathbf{X}_{(k)}$, which maps the tensor into a matrix. The (m, n, p) th element of \mathcal{X} is denoted by either x_{mnp} or $\mathcal{X}(m, n, p)$, and the vectorization of \mathcal{X} is defined as $\text{vec}(\mathcal{X}) = \text{vec}(\mathbf{X}_{(1)})$. The *Frobenius norm* of a D th-order tensor $\mathcal{X} \in \mathbb{R}^{I_1 \times \dots \times I_D}$ is defined as $\|\mathcal{X}\|_F = \sqrt{\sum_{i_1, \dots, i_D} x_{i_1, \dots, i_D}^2}$. The operator $P_\Omega : \mathbb{R}^{I_1 \times \dots \times I_D} \rightarrow \mathbb{R}^{I_1 \times \dots \times I_D}$ is the projection onto the index set Ω :

$$[P_\Omega(\mathcal{X})]_{i_1, \dots, i_D} = \begin{cases} x_{i_1, \dots, i_D}, & \text{if } (i_1, \dots, i_D) \in \Omega, \\ 0, & \text{otherwise.} \end{cases}$$

For simplicity, we alternatively denote $P_\Omega(\cdot)$ by $(\cdot)_\Omega$.

B. Smoothness Constrained Low-rank Factorization

In this section, we review several widely studied optimization problems in regularized low-rank factorization methods that incorporate side information to enforce smoothness. The standard Matrix Factorization (MF) approximates $\mathbf{Y} \in \mathbb{R}^{M \times N}$ as $\mathbf{Y} \approx \mathbf{U}\mathbf{V}^\top$, where $\mathbf{U} \in \mathbb{R}^{M \times R}$ and $\mathbf{V} \in \mathbb{R}^{N \times R}$ are lower-dimensional latent factors, with $R \ll \min\{M, N\}$ representing a pre-specified rank.

For graph-regularized MF [11], the optimization problem is formulated as

$$\min_{\mathbf{U}, \mathbf{V}} \frac{1}{2} \left\| \mathbf{Y}_\Omega - (\mathbf{U}\mathbf{V}^\top)_\Omega \right\|_F^2 + \frac{1}{2} \left(\text{tr}(\mathbf{U}^\top \mathbf{L}_U \mathbf{U}) + \text{tr}(\mathbf{V}^\top \mathbf{L}_V \mathbf{V}) \right), \quad (1)$$

where Ω denotes the set of observed entries in \mathbf{Y} . The Laplacian-based smoothness constraints are defined as

$$\mathbf{L}_U = \lambda_u \mathbf{Lap}_m + \eta_u \mathbf{I}_m, \quad \mathbf{L}_V = \lambda_v \mathbf{Lap}_N + \eta_v \mathbf{I}_N,$$

with $\{\lambda_u, \eta_u, \lambda_v, \eta_v\}$ being regularization weights and $\{\mathbf{Lap}_m, \mathbf{Lap}_N\}$ the Laplacian matrices for the respective dimensions.

In multivariate time series or spatiotemporal modeling, temporal regularization is often applied to capture temporal dependencies. For spatiotemporal data $\mathbf{Y} \in \mathbb{R}^{M \times N}$ (e.g., M spatial locations observed over N time points), the Temporal Autoregressive (AR) Regularized MF (TRMF) [15] assumes an AR model for the row vectors of the latent temporal factor matrix $\mathbf{V} = [\mathbf{v}_1, \dots, \mathbf{v}_N]^\top$. Specifically, it assumes $\mathbf{v}_n = \sum_{l \in \mathcal{L}} \mathbf{A}_l \mathbf{v}_{n-l} + \epsilon$, where \mathcal{L} is the set of time lags, $\{\mathbf{A}_l \in \mathbb{R}^{R \times R} : l \in \mathcal{L}\}$ are the coefficient matrices, and ϵ denotes white noise. The corresponding optimization problem is

$$\min_{\mathbf{U}, \mathbf{V}} \frac{1}{2} \left\| \mathbf{Y}_\Omega - (\mathbf{U}\mathbf{V}^\top)_\Omega \right\|_F^2 + \frac{\lambda_v}{2} \sum_{n=m}^T \left\| \mathbf{v}_n - \sum_{l \in \mathcal{L}} \mathbf{A}_l \mathbf{v}_{n-l} \right\|_2^2 + \frac{\eta_v}{2} \|\mathbf{V}\|_F^2 + \frac{\eta_u}{2} \|\mathbf{U}\|_F^2, \quad (2)$$

where $m = \max(\mathcal{L}) + 1$ and $\{\lambda_v, \eta_v, \eta_u\}$ are weight parameters.

Another widely applied smoothness constraint is based on total variation (TV) or quadratic variation (QV) for higher-order tensors. Given an incomplete D th-order tensor $\mathcal{Y} \in \mathbb{R}^{I_1 \times \dots \times I_D}$, the unconstrained CANDECOMP/PARAFAC (CP) decomposition [28] approximates \mathcal{Y} as $\mathcal{Y} = \sum_{r=1}^R \lambda_r \mathbf{u}_1^r \circ \dots \circ \mathbf{u}_D^r$, where R is the CP rank, λ_r is a weight, and $\mathbf{u}_d^r \in \mathbb{R}^{I_d}$ for $d = 1, \dots, D$. The TV/QV-constrained tensor CP decomposition [10] is formulated as

$$\min_{\{\lambda_r\}_{r=1}^R, \{\mathbf{U}_d\}_{d=1}^D} \frac{1}{2} \|\mathcal{Y}_\Omega - \mathcal{M}_\Omega\|_F^2 + \sum_{r=1}^R \frac{\lambda_r^2}{2} \sum_{d=1}^D \rho_d \|\mathbf{L}_d \mathbf{u}_d^r\|_p^p, \quad (3)$$

where $\mathcal{M} = \sum_{r=1}^R \lambda_r \mathbf{u}_1^r \circ \dots \circ \mathbf{u}_D^r$, and for each mode d , $\mathbf{L}_d \in \mathbb{R}^{(I_d-1) \times I_d}$ is a difference operator defined as

$$\mathbf{L}_d = \begin{bmatrix} 1 & -1 & & & \\ & 1 & -1 & & \\ & & \ddots & \ddots & \\ & & & 1 & -1 \end{bmatrix},$$

ρ_d is the smoothness parameter, and $p \in \{1, 2\}$.

While these smoothness-constrained methods effectively model low-frequency, long-range dependencies, they strictly adhere to the formulation $\mathbf{Y} = \mathbf{U}\mathbf{V}^\top + \mathbf{E}$, where the residual \mathbf{E} is assumed to be uncorrelated white noise. As a result, ignoring the local correlation structure within the

residual component may compromise the reconstruction accuracy, especially in scenarios with significant short-scale, high-frequency variations.

IV. METHODOLOGY

In this section, we introduce the proposed GLSKF framework, i.e., **Generalized Least Squares Kernelized Tensor Factorization**, for multidimensional data recovery/completion. Consider an incomplete D -dimensional data tensor $\mathcal{Y} \in \mathbb{R}^{I_1 \times \dots \times I_D}$, where Ω denotes the set of observed indices, and Ω^c denotes its complement. In GLSKF, we model the data tensor as the sum of two complementary components:

$$\mathcal{Y} \approx \mathcal{M} + \mathcal{R}, \quad (4)$$

where:

- \mathcal{M} captures the global, smoothed pattern of the data via a covariance-regularized tensor CP decomposition, i.e.,

$$\mathcal{M} = \sum_{r=1}^R \mathbf{u}_1^r \circ \mathbf{u}_2^r \circ \dots \circ \mathbf{u}_D^r, \quad (5)$$

with R being a pre-specified rank and $\mathbf{u}_d^r \in \mathbb{R}^{I_d}$ denoting the r th column of the latent factor matrix for the d th dimension.

- \mathcal{R} models the local structure via a locally covariance-constrained tensor.

We capture the correlations in both \mathcal{M} and \mathcal{R} through constraints based on covariance matrices. Next, we define a regularization norm—the covariance norm (or \mathbf{K} -norm)—that imposes smoothness constraints, and then introduce the objective function of GLSKF for data completion.

Definition 1 (Covariance Norm). Given a vector $\mathbf{x} \in \mathbb{R}^M$ and a positive semi-definite (PSD) covariance matrix $\mathbf{K}_x \in \mathbb{R}^{M \times M}$, the covariance norm (or \mathbf{K} -norm) for \mathbf{x} is defined as:

$$\|\mathbf{x}\|_{\mathbf{K}_x} := \sqrt{\mathbf{x}^\top \mathbf{K}_x^{-1} \mathbf{x}}.$$

For a matrix $\mathbf{X} \in \mathbb{R}^{M \times N}$, given covariance matrices $\mathbf{K}_1 \in \mathbb{R}^{M \times M}$ and $\mathbf{K}_2 \in \mathbb{R}^{N \times N}$, the \mathbf{K} -norm is defined as:

$$\|\mathbf{X}\|_{\mathbf{K}_1, \mathbf{K}_2} := \sqrt{\text{tr}(\mathbf{K}_2^{-1} \mathbf{X}^\top \mathbf{K}_1^{-1} \mathbf{X})},$$

which is equivalent to

$$\|\text{vec}(\mathbf{X})\|_{\mathbf{K}_2 \otimes \mathbf{K}_1} = \sqrt{\text{vec}(\mathbf{X})^\top (\mathbf{K}_2^{-1} \otimes \mathbf{K}_1^{-1}) \text{vec}(\mathbf{X})}.$$

For a third-order tensor, the covariance norm is defined using either the matricized or vectorized form of the tensor, along with corresponding covariance matrices for each dimension. Suppose $\mathcal{X} \in \mathbb{R}^{M \times N \times P}$ is constrained by a product covariance function based on covariance matrices $\mathbf{K}_1 \in \mathbb{R}^{M \times M}$, $\mathbf{K}_2 \in \mathbb{R}^{N \times N}$, and $\mathbf{K}_3 \in \mathbb{R}^{P \times P}$ for the three dimensions. Then, the covariance norm of \mathcal{X} is given by:

$$\begin{aligned} \|\mathcal{X}\|_{\mathbf{K}_1, \mathbf{K}_2, \mathbf{K}_3} &= \sqrt{\text{tr}((\mathbf{K}_3^{-1} \otimes \mathbf{K}_2^{-1}) \mathbf{X}_{(1)}^\top \mathbf{K}_1^{-1} \mathbf{X}_{(1)})} \\ &= \sqrt{\text{vec}(\mathcal{X})^\top (\mathbf{K}_3^{-1} \otimes \mathbf{K}_2^{-1} \otimes \mathbf{K}_1^{-1}) \text{vec}(\mathcal{X})}. \end{aligned}$$

The covariance norm for higher-order tensors is defined analogously. For simplicity, we equivalently denote $\|\mathbf{X}\|_{\mathbf{K}_1, \mathbf{K}_2}$ as $\|\mathbf{X}\|_{\mathbf{K}_X}$ with $\mathbf{K}_X = \mathbf{K}_2 \otimes \mathbf{K}_1$ and $\|\mathcal{X}\|_{\mathbf{K}_1, \mathbf{K}_2, \mathbf{K}_3}$ as $\|\mathcal{X}\|_{\mathbf{K}_X}$ with $\mathbf{K}_X = \mathbf{K}_3 \otimes \mathbf{K}_2 \otimes \mathbf{K}_1$ for matrix \mathbf{X} and third-order tensor \mathcal{X} .

The covariance norm can be interpreted as a generalized form of the Mahalanobis distance. Notably, it serves as a versatile smoothness constraint; many regularization terms studied in the literature can be expressed as special cases of the covariance norm with appropriate choices of covariance matrices. For example, by setting $\mathbf{K}_d^{-1} = \mathbf{L}_d^\top \mathbf{L}_d$, where \mathbf{L}_d is the differentiation operator defined in Eq. (3), the smoothness constraint imposed on the latent factors in QV-regularized SPC [10] (i.e., $\|\mathbf{L}_d \mathbf{u}_d^r\|_2^2$) is equivalent to the covariance norm with covariance matrix \mathbf{K}_d :

$$\|\mathbf{u}_d^r\|_{\mathbf{K}_d}^2 = (\mathbf{u}_d^r)^\top \mathbf{K}_d^{-1} \mathbf{u}_d^r.$$

Furthermore, when the covariance matrix is the identity matrix, the covariance norm reduces to the standard ℓ_2 norm for vectors or the Frobenius norm for matrices. This demonstrates that the covariance norm provides a unifying framework for various smoothness constraints.

When the covariance structure of the local component is specified, the global component \mathcal{M} can, in principle, be estimated in closed form via generalized least squares by marginalizing the correlated errors. However, this approach is computationally prohibitive, as it requires computing the inverse of an $|\Omega| \times |\Omega|$ matrix. Therefore, we propose to explicitly learn the local component \mathcal{R} rather than marginalizing it. This formulation leverages the flexibility of the covariance norm to efficiently capture both global structures and local dependencies.

A. Optimization Problem

The optimization problem of GLSKF for recovery of a D -dimensional tensor \mathcal{Y} is formulated as:

$$\begin{aligned} \min_{\{\mathbf{U}_d\}_{d=1}^D, \mathcal{R}} & \frac{1}{2} \|\mathcal{Y}_\Omega - \mathcal{M}_\Omega - \mathcal{R}_\Omega\|_F^2 \\ & + \sum_{d=1}^D \frac{\rho}{2} \|\mathbf{U}_d\|_{\mathbf{K}_d^U}^2 + \frac{\gamma}{2} \|\mathcal{R}\|_{\mathbf{K}_R}^2, \end{aligned} \quad (6)$$

where

- $\mathbf{K}_d^U = \mathbf{I}_d \otimes \mathbf{K}_d^u \in \mathbb{R}^{(RI_d) \times (RI_d)}$ is the covariance matrix added on the latent factor matrix \mathbf{U}_d for $d = 1, \dots, D$, with $\mathbf{K}_d^u \in \mathbb{R}^{I_d \times I_d}$ being the covariance for each column of \mathbf{U}_d , i.e., $\{\mathbf{u}_d^r : r = 1, \dots, R\}$,
- $\mathbf{K}_R = \bigotimes_{d=D}^1 \mathbf{K}_d^r \in \mathbb{R}^{N \times N}$ denotes the covariance placed on \mathcal{R} with $\mathbf{K}_d^r \in \mathbb{R}^{I_d \times I_d}$ being the covariance for the d th dimension of the local component,
- and ρ and γ are penalty parameters on the global latent factors and the local component, respectively.

Here, the first term constrains the reconstruction error on the observed data, while the covariance constraints $\|\mathbf{U}_d\|_{\mathbf{K}_d^U}^2$ and $\|\mathcal{R}\|_{\mathbf{K}_R}^2$ can be interpreted as imposing Gaussian priors $\mathcal{N}(\mathbf{0}, \mathbf{K}_d^U)$ and $\mathcal{N}(\mathbf{0}, \mathbf{K}_R)$ on \mathbf{U}_d and \mathcal{R} , respectively. We denote this objective function by $\mathcal{F}(\{\mathbf{U}_d : d = 1, \dots, D\}, \mathcal{R})$.

For better representation, we introduce related notations for indexing missing and observed entries. Let $\mathcal{O} \in \mathbb{R}^{I_1 \times \dots \times I_D}$ be a binary indicator tensor defined by

$$o_{i_1 \dots i_D} = \begin{cases} 1, & \text{if } (i_1, \dots, i_D) \in \Omega, \\ 0, & \text{otherwise.} \end{cases}$$

Denote by $\mathbf{O}_{(d)} \in \mathbb{R}^{I_d \times \frac{N}{I_d}}$ the mode- d unfolding of \mathcal{O} , where $N = \prod_{d=1}^D I_d$. Define the binary matrices $\mathbf{O}_d \in \mathbb{R}^{|\Omega| \times N}$ and $\mathbf{O}_d^c \in \mathbb{R}^{|\Omega^c| \times N}$ with $|\Omega| + |\Omega^c| = N$ by selecting the rows corresponding to ones and zeros, respectively, in $\text{vec}(\mathbf{O}_{(d)})$ from the $N \times N$ identity matrix \mathbf{I}_N . Thus, $\mathbf{O}_d \times (\cdot) : \mathbb{R}^N \rightarrow \mathbb{R}^{|\Omega|}$ and $\mathbf{O}_d^c \times (\cdot) : \mathbb{R}^{|\Omega|} \rightarrow \mathbb{R}^N$ perform slicing and zero-padding on a vectorized full tensor and its incomplete counterpart, respectively, along the d th dimension.

The covariance matrices $\{\mathbf{K}_d^u, \mathbf{K}_d^r : d = 1, \dots, D\}$ are derived from valid kernel functions [22]. For example, the squared exponential (SE) kernel

$$k_{SE}(x_i, x_j; l, \sigma) = \sigma^2 \exp\left(-\frac{\|x_i - x_j\|_2^2}{2l^2}\right)$$

(with length-scale l and variance σ^2) is a common choice. The specification of these covariance matrices is critical, as the variable updates in Alternating Least Squares (ALS) involve solving linear systems whose sizes depend directly on these matrices. To enhance computational efficiency, GLSKF employs sparse covariance or precision matrices. In particular, the local covariance \mathbf{K}_d^r can be constructed as a sparse, banded matrix using covariance tapering [29], [30], or its inverse (the precision matrix $\mathbf{\Lambda}_d^r = (\mathbf{K}_d^r)^{-1}$) can be specified as sparse based on Gaussian Markov random fields (GMRFs) [31]. Such strategies are especially effective when $|\Omega|$ is much smaller than N .

B. Model Solution

The optimization problem in Eq. (6) is solved via an alternating least squares (ALS) procedure. To update the global component \mathcal{M} , we fix the local component \mathcal{R} , and update the latent matrices $\{\mathbf{U}_d : d = 1, \dots, D\}$ one dimension at a time. In particular, we optimize the following local objective function for the latent factors:

$$\mathcal{F}_{\mathbf{U}_d}(\{\mathbf{U}_d\}_{d=1}^D, \mathcal{R}) = \frac{1}{2} \left\| \mathcal{G}_\Omega - \mathcal{M}_\Omega \right\|_F^2 + \frac{\rho}{2} \sum_{d=1}^D \left\| \mathbf{U}_d \right\|_{\mathbf{K}_d^u}^2, \quad (7)$$

where $\mathcal{G}_\Omega = \mathcal{Y}_\Omega - \mathcal{R}_\Omega$. When $D = 2$, this problem is equivalent to that in GRALS [11], which is solved using the conjugate gradient (CG) method. Here, we generalize the approach to higher-order tensors and general covariance constraints.

To update the observed local component \mathcal{R} , assuming that \mathcal{M} is known, we define a local objective function:

$$\mathcal{F}_{\mathcal{R}}(\mathcal{R}, \mathcal{M}) = \frac{1}{2} \left\| \mathcal{L}_\Omega - \mathcal{R}_\Omega \right\|_F^2 + \frac{\gamma}{2} \left\| \mathcal{R} \right\|_{\mathbf{K}_{\mathcal{R}}}^2, \quad (8)$$

with $\mathcal{L}_\Omega = \mathcal{Y}_\Omega - \mathcal{M}_\Omega$.

At each iteration $k+1$, the variables are updated as follows:

$$\begin{cases} \mathbf{U}_d^{(k+1)} &= \arg \min_{\mathbf{U}_d} \mathcal{F}_{\mathbf{U}_d}(\mathbf{U}_1^{(k+1)}, \dots, \mathbf{U}_{d-1}^{(k+1)}, \\ &\quad \mathbf{U}_d, \mathbf{U}_{d+1}^{(k)}, \dots, \mathbf{U}_D^{(k)}, \mathcal{R}^{(k)}), \quad d = 1, \dots, D, \\ \mathcal{M}^{(k+1)} &= \sum_{r=1}^R (\mathbf{u}_1^r)^{(k+1)} \circ \dots \circ (\mathbf{u}_D^r)^{(k+1)}, \\ \mathcal{R}^{(k+1)} &= \arg \min_{\mathcal{R}} \mathcal{F}_{\mathcal{R}}(\mathcal{R}, \mathcal{M}^{(k+1)}). \end{cases} \quad (9)$$

The complete estimation tensor is given by $\hat{\mathcal{Y}} = \mathcal{M} + \mathcal{R}$. Below, we detail the computational solutions for updating each variable.

1) *Update Global Latent Factors* $\{\mathbf{U}_d : d = 1, \dots, D\}$:

For a given d , we solve for the latent matrix \mathbf{U}_d by minimizing

$$\min_{\mathbf{U}_d} \frac{1}{2} \left\| \mathcal{G}_\Omega - \mathcal{M}_\Omega \right\|_F^2 + \frac{\rho}{2} \left\| \mathbf{U}_d \right\|_{\mathbf{K}_d^u}^2. \quad (10)$$

Using the CP decomposition in Eq. (5), the mode- d unfolding satisfies

$$\mathbf{M}_{(d)}^\top = (\mathbf{U}_D \circ \dots \circ \mathbf{U}_{d+1} \circ \mathbf{U}_{d-1} \circ \dots \circ \mathbf{U}_1) \mathbf{U}_d^\top.$$

Exploiting the identity $\text{vec}(\mathbf{A}\mathbf{X}\mathbf{B}) = (\mathbf{B}^\top \otimes \mathbf{A}) \text{vec}(\mathbf{X})$, we write

$$\text{vec}(\mathbf{M}_{(d)}^\top) = \left(\mathbf{I}_{I_d} \otimes (\mathbf{U}_D \circ \dots \circ \mathbf{U}_{d+1} \circ \mathbf{U}_{d-1} \circ \dots \circ \mathbf{U}_1) \right) \text{vec}(\mathbf{U}_d^\top). \quad (11)$$

Let $\mathbf{O}'_d \in \mathbb{R}^{|\Omega| \times N}$ be the binary matrix obtained by selecting the rows corresponding to ones in $\text{vec}(\mathbf{O}_{(d)}^\top)$ from the $N \times N$ identity. Then the sub-problem for \mathbf{U}_d can be written as

$$\begin{aligned} \min_{\mathbf{U}_d} \frac{1}{2} \left\| \mathbf{O}'_d \text{vec}(\mathbf{G}_{(d)}^\top) - \mathbf{O}'_d \mathbf{H}_d \text{vec}(\mathbf{U}_d^\top) \right\|_2^2 \\ + \frac{\rho}{2} \text{vec}(\mathbf{U}_d^\top)^\top (\mathbf{K}_d^u \otimes \mathbf{I}_R)^{-1} \text{vec}(\mathbf{U}_d^\top), \end{aligned} \quad (12)$$

where \mathbf{H}_d is defined as

$$\begin{aligned} \mathbf{H}_d &= \mathbf{I}_{I_d} \otimes \mathbf{H}_d^u \in \mathbb{R}^{N \times (RI_d)}, \quad \text{with} \\ \mathbf{H}_d^u &= \mathbf{U}_D^{(k)} \circ \dots \circ \mathbf{U}_{d+1}^{(k)} \circ \mathbf{U}_{d-1}^{(k+1)} \circ \dots \circ \mathbf{U}_1^{(k+1)} \in \mathbb{R}^{\frac{N}{I_d} \times R}. \end{aligned} \quad (13)$$

The term $\mathbf{O}'_d \mathbf{H}_d \text{vec}(\mathbf{U}_d^\top)$ is equivalent to $\mathbf{O}'_d \text{vec}(\mathbf{M}_{(d)}^\top)$, and $\mathbf{K}_d^u \otimes \mathbf{I}_R$ is the covariance for $\text{vec}(\mathbf{U}_d^\top)$.

Taking the gradient of the objective in Eq. (12) with respect to $\text{vec}(\mathbf{U}_d^\top)$ and setting it to zero yields the linear system

$$\begin{aligned} \text{vec} \left((\mathbf{U}_d^{(k+1)})^\top \right) &= \underbrace{\left(\mathbf{H}_d^\top \mathbf{O}'_d{}^\top \mathbf{O}'_d \mathbf{H}_d + \rho (\mathbf{K}_d^u)^{-1} \otimes \mathbf{I}_R \right)}_{\mathbf{A}_1} \underbrace{\text{vec}(\mathbf{G}_{(d)}^\top)}_{\mathbf{A}_2} \\ &\quad \underbrace{\times \mathbf{H}_d^\top \mathbf{O}'_d{}^\top \mathbf{O}'_d \text{vec}(\mathbf{G}_{(d)}^\top)}_{\mathbf{b} \in \mathbb{R}^{RI_d}}. \end{aligned} \quad (14)$$

where $\mathbf{A}_1, \mathbf{A}_2 \in \mathbb{R}^{(RI_d) \times (RI_d)}$ and $\mathbf{b} \in \mathbb{R}^{RI_d}$. We solve Eq. (14) using the conjugate gradient (CG) method, which requires repeated evaluations of the matrix-vector products $\mathbf{A}_1 \times (\cdot)$ and $\mathbf{A}_2 \times (\cdot)$.

Algorithm 1 CG for solving \mathbf{U}_d , i.e., Eq. (14).

Input: $\mathbf{U}_1^{(k+1)}, \dots, \mathbf{U}_{d-1}^{(k+1)}, \mathbf{U}_{d+1}^{(k)}, \dots, \mathbf{U}_D^{(k)}, (\mathbf{K}_d^u)^{-1}$, maximum number of iterations $J = 1000$.

Output: $\mathbf{U}_d^{(k+1)}$.

- 1: Compute the vector right-side the inverse, i.e., $\mathbf{b} = \mathbf{H}_d^\top \mathbf{O}_d'^\top \mathbf{O}_d' \text{vec}(\mathbf{G}_{(d)}^\top) = \mathbf{H}_d^\top \text{vec}([\mathcal{G} * \mathcal{O}]_{(d)}^\top)$;
 - 2: Let $\mathbf{x}_0 = \text{vec}\left(\left(\mathbf{U}_d^{(k)}\right)^\top\right) \in \mathbb{R}^{RI_d}$, $\mathbf{A} = \mathbf{A}_1 + \mathbf{A}_2 \in \mathbb{R}^{(RI_d) \times (RI_d)}$ as defined in Eq. (14);
 - 3: Compute $\mathbf{A}\mathbf{x}_0$;
 - 4: Compute the initial residual $\mathbf{e}_0 = \mathbf{b} - \mathbf{A}\mathbf{x}_0$;
 - 5: Let the direction $\mathbf{p}_1 = \mathbf{e}_0$;
 - 6: **for** $j = 1$ **to** J_{CG}^U **do**
 - 7: Compute $\mathbf{A}\mathbf{p}_j = \mathbf{A}_1\mathbf{p}_j + \mathbf{A}_2\mathbf{p}_j$; $\mathcal{O}(R|\Omega| + RI_d^2)$
 - 8: Compute the step size $\alpha_j = \frac{\mathbf{e}_{j-1}^\top \mathbf{e}_{j-1}}{\mathbf{p}_j^\top (\mathbf{A}\mathbf{p}_j)}$;
 - 9: Compute the updated solution $\mathbf{x}_j = \mathbf{x}_{j-1} + \alpha_j \mathbf{p}_j$;
 - 10: Compute residual $\mathbf{e}_j = \mathbf{e}_{j-1} - \alpha_j (\mathbf{A}\mathbf{p}_j)$;
 - 11: **if** $\sqrt{\mathbf{e}_j^\top \mathbf{e}_j} < 10^{-6}$ **then**
 - 12: **break**;
 - 13: **end if**
 - 14: Compute $\beta_j = \frac{\mathbf{e}_j^\top \mathbf{e}_j}{\mathbf{e}_{j-1}^\top \mathbf{e}_{j-1}}$;
 - 15: Compute the direction $\mathbf{p}_{j+1} = \mathbf{e}_j + \beta_j \mathbf{p}_j$;
 - 16: **end for**
 - 17: **return** $\mathbf{U}_d^{(k+1)} = (\text{reshape}(\mathbf{x}_j, [R, I_d]))^\top$.
-

Notice that $\mathbf{A}_1 = \mathbf{H}_d^\top \mathbf{O}_d'^\top \mathbf{O}_d' \mathbf{H}_d$ has a block-diagonal structure because $\mathbf{O}_d'^\top \mathbf{O}_d'$ is a sparse diagonal matrix (i.e., $\text{diag}(\text{vec}(\mathbf{O}_{(d)}^\top))$). Consequently, computing $\mathbf{A}_1 \times (\cdot)$ requires only $\mathcal{O}(R|\Omega|)$ operations. For $\mathbf{A}_2 = \rho (\mathbf{K}_d^u)^{-1} \otimes \mathbf{I}_R$, we leverage the Kronecker matrix–vector multiplication (MVM) property to compute $\mathbf{A}_2 \times (\cdot)$ efficiently with cost $\mathcal{O}(RI_d^2)$.

Thus, the per-iteration cost for the CG solution is $\mathcal{O}(R|\Omega| + RI_d^2)$. Moreover, if we construct $(\mathbf{K}_d^u)^{-1}$ as a sparse precision matrix (e.g., via a GMRF), the cost of $\mathbf{A}_2 \times (\cdot)$ can be further reduced to $\mathcal{O}(R\omega((\mathbf{K}_d^u)^{-1}))$, where $\omega(\cdot)$ denotes the number of nonzero elements.

We initialize the CG iterations with the previous iterate $\text{vec}\left(\left(\mathbf{U}_d^{(k)}\right)^\top\right)$ to accelerate convergence. Algorithm 1 details the CG procedure for updating \mathbf{U}_d . Overall, the computational cost for updating the latent matrices using CG is $\mathcal{O}(J_{\text{CG}}^U (R|\Omega| + RI_d^2))$, where $J_{\text{CG}}^U \ll RI_d$ is the number of CG iterations required for convergence. This linear cost is much cheaper than directly computing the closed-form solution in Eq. (14), which would cost $\mathcal{O}((RI_d)^3)$. It is also worth noting that for image or video data, the covariance matrices for the two spatial dimensions are typically generated by applying a stationary kernel on a 1D regular grid. In such cases, one can further reduce the computational cost by exploiting the Toeplitz structure of the covariance matrices for fast matrix–vector multiplication (MVM) [32], achieving a cost of $\mathcal{O}(RI_d \log(I_d))$.

2) *Update Local Component \mathcal{R}* : We update the local component tensor \mathcal{R} based on $\mathcal{F}_{\mathcal{R}}$ in Eq. (8):

$$\min_{\mathcal{R}} \frac{1}{2} \|\mathcal{L}_\Omega - \mathcal{R}\|_F^2 + \frac{\gamma}{2} \|\mathcal{R}\|_{\mathbf{K}_{\mathcal{R}}}^2. \quad (15)$$

Define $\mathbf{l}_o = \mathbf{O}_1 \text{vec}(\mathcal{L}_\Omega) \in \mathbb{R}^{|\Omega|}$ and $\mathbf{r} = \text{vec}(\mathcal{R}) \in \mathbb{R}^N$. The optimization problem can be transformed into a Tikhonov-regularized least squares problem:

$$\min_{\mathbf{r}} \frac{1}{2} \|\mathbf{l}_o - \mathbf{O}_1 \mathbf{r}\|_2^2 + \frac{\gamma}{2} \|\mathbf{r}\|_{\mathbf{K}_r}^2, \quad (16)$$

where $\mathbf{K}_r = \bigotimes_{d=D}^1 \mathbf{K}_d^r$. Setting the gradient with respect to \mathbf{r} , $(\mathbf{O}_1^\top \mathbf{O}_1 + \gamma \mathbf{K}_r^{-1}) \mathbf{r} - \mathbf{O}_1^\top \mathbf{l}_o$, to $\mathbf{0}$, we have the closed-form solution of \mathbf{r} :

$$\mathbf{r} = \left(\mathbf{O}_1^\top \mathbf{O}_1 + \gamma \mathbf{K}_r^{-1}\right)^{-1} \mathbf{O}_1^\top \mathbf{l}_o. \quad (17)$$

Computing \mathbf{r} using Eq. (17) requires solving an $N \times N$ linear system, which is computationally expensive. One approach to reduce this cost is to model \mathbf{r} using a Gaussian Markov random field (GMRF) [31], which yields a sparse precision matrix $\mathbf{\Lambda}_r = \mathbf{K}_r^{-1}$ that exhibits a banded structure after an appropriate permutation. In the general case, we leverage the dual form of Tikhonov regularization by introducing a dual variable $\mathbf{z} \in \mathbb{R}^{|\Omega|}$ and setting $\mathbf{r} = \mathbf{K}_r \mathbf{O}_1^\top \mathbf{z}$. By replacing the decision variable with \mathbf{z} , the optimization problem becomes

$$\min_{\mathbf{z}} \frac{1}{2} \|\mathbf{l}_o - \mathbf{O}_1 \mathbf{K}_r \mathbf{O}_1^\top \mathbf{z}\|_2^2 + \frac{\gamma}{2} \mathbf{z}^\top \mathbf{O}_1 \mathbf{K}_r \mathbf{O}_1^\top \mathbf{z}. \quad (18)$$

The derivative of the objective function with respect to \mathbf{z} is $\mathbf{O}_1 \mathbf{K}_r \mathbf{O}_1^\top \left((\mathbf{O}_1 \mathbf{K}_r \mathbf{O}_1^\top + \gamma \mathbf{I}_{|\Omega|}) \mathbf{z} - \mathbf{l}_o \right)$. Thus, by setting the derivative to $\mathbf{0}$, the optimal \mathbf{z} is given by

$$\mathbf{z} = \left(\mathbf{O}_1 \mathbf{K}_r \mathbf{O}_1^\top + \gamma \mathbf{I}_{|\Omega|}\right)^{-1} \mathbf{l}_o. \quad (19)$$

Consequently, the solution for \mathbf{r} at iteration k becomes

$$\mathbf{r}^{(k+1)} = \mathbf{K}_r \mathbf{O}_1^\top \underbrace{\left(\mathbf{O}_1 \mathbf{K}_r \mathbf{O}_1^\top + \gamma \mathbf{I}_{|\Omega|}\right)^{-1}}_{\mathbf{A}_3} \mathbf{l}_o^{(k+1)}. \quad (20)$$

$\mathbf{z}^{(k+1)} \in \mathbb{R}^{|\Omega|}$

Compared to Eq. (17), the solution in Eq. (20) is computationally more efficient, as it only requires solving for $\mathbf{z}^{(k+1)}$ in an $|\Omega| \times |\Omega|$ linear system, which can be efficiently obtained using the CG method. In the CG algorithm, given a vector $\mathbf{x} \in \mathbb{R}^{|\Omega|}$, the product

$$\mathbf{A}_3 \mathbf{x} = \mathbf{O}_1 \mathbf{K}_{\mathcal{R}} \mathbf{O}_1^\top \mathbf{x}$$

is computed efficiently by performing a series of matrix–vector multiplications: first, \mathbf{O}_1^\top zero-pads \mathbf{x} to a length- N vector; then, the multiplication by $\mathbf{K}_{\mathcal{R}}$ is executed via Kronecker MVM; finally, \mathbf{O}_1 slices the result back to $\mathbb{R}^{|\Omega|}$. The computational cost of solving Eq. (20) is $\mathcal{O}\left(J_{\text{CG}}^z \sum_{d=1}^D \left(\omega(\mathbf{K}_d^r) \frac{N}{I_d}\right)\right)$. Algorithm 2 provides the computation procedure for updating $\mathcal{R}^{(k+1)}$ with Eq. (20).

Finally, note that, due to the additive structure of GLSKF, in practice we first update the latent factors \mathbf{U}_d for several iterations with the local component set to zero, and then incorporate \mathcal{R} into the optimization to improve convergence.

Algorithm 2 Updating $\mathcal{R}^{(k+1)}$ with Eq. (20).

Input: $\mathbf{l}_o^{(k+1)}$, $\{\mathbf{K}_d^r : d = 1, \dots, D\}$, maximum number of iterations $J = 1000$.

Output: $\mathcal{R}^{(k+1)}$.

- 1: Let $\mathbf{b} = \mathbf{l}_o^{(k+1)} \in \mathbb{R}^{|\Omega|}$;
 - 2: Let $\mathbf{x}_0 = \mathbf{z}^{(k)} \in \mathbb{R}^{|\Omega|}$, $\mathbf{A} = \gamma \mathbf{I}_{|\Omega|} + \mathbf{A}_3 \in \mathbb{R}^{|\Omega| \times |\Omega|}$ with $\mathbf{A}_3 = \mathbf{O}_1 \mathbf{K}_r \mathbf{O}_1^\top$ as given in Eq. (20);
 - 3: Compute $\mathbf{A}\mathbf{x}_0 = \gamma \mathbf{x}_0 + \mathbf{A}_3 \mathbf{x}_0$, where $\mathbf{A}_3 \mathbf{x}_0$ is computed as $\mathbf{O}_1 \mathbf{K}_r \mathbf{O}_1^\top \mathbf{x}_0$ from right to left via zero-padding: $\mathbf{O}_1^\top \mathbf{x}_0$, Kronecker MVM: $\mathbf{K}_r \times (\cdot)$, and slicing: $\mathbf{O}_1 \times (\cdot)$;
 - 4: Compute the initial residual $\mathbf{e}_0 = \mathbf{b} - \mathbf{A}\mathbf{x}_0 \in \mathbb{R}^{|\Omega|}$;
 - 5: Let the direction $\mathbf{p}_1 = \mathbf{e}_0$;
 - 6: **for** $j = 1$ **to** J_{CG}^z **do**
 - 7: Compute $\mathbf{A}\mathbf{p}_j = \gamma \mathbf{p}_j + \mathbf{A}_3 \mathbf{p}_j$, where $\mathbf{A}_3 \mathbf{p}_j$ is computed similarly as $\mathbf{A}_3 \mathbf{x}_0$; $\mathcal{O}\left(\sum_d \left(\omega(\mathbf{K}_d^r) \frac{N}{I_d}\right)\right)$
 - 8: Compute the step size $\alpha_j = \frac{\mathbf{e}_{j-1}^\top \mathbf{e}_{j-1}}{\mathbf{p}_j^\top (\mathbf{A}\mathbf{p}_j)}$;
 - 9: Compute the updated solution $\mathbf{x}_j = \mathbf{x}_{j-1} + \alpha_j \mathbf{p}_j$;
 - 10: Compute residual $\mathbf{e}_j = \mathbf{e}_{j-1} - \alpha_j (\mathbf{A}\mathbf{p}_j)$;
 - 11: **if** $\sqrt{\mathbf{e}_j^\top \mathbf{e}_j} < 10^{-6}$ **then**
 - 12: **break**;
 - 13: **end if**
 - 14: Compute $\beta_j = \frac{\mathbf{e}_j^\top \mathbf{e}_j}{\mathbf{e}_{j-1}^\top \mathbf{e}_{j-1}}$;
 - 15: Compute the direction $\mathbf{p}_{j+1} = \mathbf{e}_j + \beta_j \mathbf{p}_j$;
 - 16: **end for**
 - 17: $\mathbf{z}^{(k+1)} = \mathbf{x}_j$;
 - 18: Compute $\mathbf{r}^{(k+1)} = \mathbf{K}_r \mathbf{O}_1^\top \mathbf{z}^{(k+1)}$ by Kronecker MVM;
 - 19: **return** $\mathcal{R}^{(k+1)} = \text{reshape}(\mathbf{r}^{(k+1)}, \text{size}(\mathcal{R}))$.
-

C. Model Parameters

The proposed GLSKF model involves several types of model parameters and hyperparameters:

(i) **Covariance Matrices** $\{\mathbf{K}_d^u, \mathbf{K}_d^r : d = 1, \dots, D\}$. These matrices are used to enforce the covariance norm constraints. For dimensions $d = 1, \dots, D - 1$, we assume that \mathbf{K}_d^u and \mathbf{K}_d^r are correlation matrices computed from valid kernel functions. The kernel length-scale hyperparameters are selected empirically, with the variances fixed to 1. For the last dimension ($d = D$), which typically represents features or channels without inherent correlations, we set $\mathbf{K}_D^u = \mathbf{I}_{I_D}$ (i.e., assume independence). The matrix \mathbf{K}_D^r may be updated in each iteration as the covariance of $\mathbf{R}_{(D)}$ (the mode- D unfolding of \mathcal{R}); alternatively, it can be fixed as the identity matrix \mathbf{I}_{I_D} .

(ii) **Weight Parameters ρ and γ** . The parameters ρ and γ serve as regularization weights for the global latent factors and the local component tensor, respectively. They control the trade-off between the two components in the model. In practice, these parameters are tuned based on available ground truth.

(iii) **Tensor CP Rank R** . The integration of the local component in GLSKF reduces the required tensor rank, thereby decreasing computational complexity. Since the local component effectively captures detailed information and local correlations, a lower rank suffices for the global factors. In our

Algorithm 3 GLSKF for data completion.

Input: \mathcal{Y}_Ω , ρ , γ , R .

Output: Completed tensor $\hat{\mathcal{Y}}$.

- 1: Initialize $\{\mathbf{U}_d : d = 1, \dots, D\}$ as small random values; initialize \mathcal{R} as a zero-tensor.
 - 2: **for** $k = 0$ **to** $K - 1$ **do**
 - 3: **for** $d = 1$ **to** D **do**
 - 4: Update $\mathbf{U}_d^{(k+1)}$ by Eq. (14), Algorithm 1;
 $\mathcal{O}\left(\mathcal{J}_{\text{CG}}(R|\Omega| + RI_d^2)\right)$
 - 5: **end for**
 - 6: **if** $k \geq K_0$ **then**
 - 7: Update $\mathcal{M}^{(k+1)}$ by Eq. (9);
 - 8: Update $\mathcal{R}^{(k+1)}$ by Eq. (20), Algorithm 2;
 $\mathcal{O}\left(\mathcal{J}_{\text{CG}} \sum_d \left(\omega(\mathbf{K}_d^r) \frac{N}{I_d}\right)\right)$
 - 9: Compute $\mathbf{K}_D^r = \text{cov}\left(\mathbf{R}_{(3)}^{(k+1)}\right)$, update \mathbf{K}_R ;
 - 10: **end if**
 - 11: **if** Converged by stopping criteria **then**
 - 12: **break**;
 - 13: **end if**
 - 14: **end for**
 - 15: **return** $\hat{\mathcal{Y}}$ by Eq. (21).
-

experiments, the rank is set empirically.

D. Model Implementation

There are several key considerations for the overall implementation of GLSKF. First, due to its additive structure, jointly estimating the global component \mathcal{M} and the local component \mathcal{R} from a random initialization can be challenging. To facilitate convergence, we initialize the entire local component \mathcal{R} as a zero tensor and focus solely on estimating the global component \mathcal{M} for the first K_0 iterations (with $K_0 < K$). This staged strategy ensures that the local component is updated only after the global component has been reliably learned, leading to more stable and efficient optimization.

Second, we typically initialize with $\mathbf{K}_D^r = \mathbf{I}_{I_d}$, which however may not reflect the true data distribution. After the local component has been updated, we compute an empirical \mathbf{K}_D^r from the current estimate of \mathcal{R} , and this updated \mathbf{K}_D^r is incorporated into the optimization problem for \mathcal{R} . With the estimates $\mathcal{M}^{(k+1)}$ and $\mathcal{R}^{(k+1)}$, the completed estimation tensor $\hat{\mathcal{Y}}$ is updated as follows:

$$\hat{\mathcal{Y}}_\Omega = \mathcal{Y}_\Omega, \quad \hat{\mathcal{Y}}_{\Omega^c} = \mathcal{M}_{\Omega^c}^{(k+1)} + \mathcal{R}_{\Omega^c}^{(k+1)}. \quad (21)$$

For convergence, we monitor the change in the reconstruction over the observed entries and stop when

$$\|\mathcal{Y}_\Omega^{(k+1)} - \mathcal{Y}_\Omega^{(k)}\|_F^2 < \epsilon,$$

where ϵ is a predefined threshold. The overall GLSKF implementation for multidimensional data recovery is summarized in Algorithm 3.

E. Computational Complexity

We compare the theoretical model complexities of various solutions for missing data completion in Table I. The proposed

TABLE I: Comparison of model complexity.

Solution	Global cost [Model]	Local cost [Model]
Gradient descent	$\mathcal{O}(J_{\text{GD}} R \sum_d I_d^2)$ [SPC [10]]	$\mathcal{O}(J_{\text{GD}} \Omega ^2)$
Conjugate gradient	$\mathcal{O}(J_{\text{CG}}(R \Omega + R\omega(\mathbf{L}_U)))$ [GRALS [11]]	$\mathcal{O}(J_{\text{CG}} \Omega ^2)$
Closed-form	$\mathcal{O}(\sum_d (RI_d)^3)$ [Eq. (14)]	$\mathcal{O}(\Omega ^3)$ [Eq. (20)]
CG with $\mathbf{O}_d, \mathbf{O}_d^\top$	$\mathcal{O}(J_{\text{CG}}(R \Omega + RI_d^2))$ [GLSKF]	$\mathcal{O}(J_{\text{CG}} \sum_d \omega(\mathbf{K}_d^r) \frac{N}{I_d})$ [GLSKF]

Generally $J_{\text{GD}} > J_{\text{CG}}$,

\mathbf{L}_U is the regularization matrix for GRALS in Eq. (1).

GLSKF framework fully exploits Kronecker matrix–vector multiplications, sparse matrix computations, and the inherent structure of the data to achieve linear complexity. Moreover, by effectively capturing local correlations via its local component, GLSKF requires a significantly lower rank R than other low-rank methods, further enhancing its computational efficiency.

V. EXPERIMENTS

In this section, we evaluate the performance of the proposed GLSKF framework for multidimensional data completion on four real-world problems: (i) highway traffic speed data imputation, (ii) color image inpainting, (iii) fourth-order color video completion, and (iv) MRI image completion. Sampling rate is defined as $\text{SR} = \frac{|\Omega|}{N} = \frac{|\Omega|}{\prod_{d=1}^D I_d}$. All experiments are conducted on a machine with a 16-core Intel Core 2.40 GHz CPU and 32 GB RAM. The experimental code is publicly available at <https://github.com/MengyingLei/GLSKF>.

For (i) traffic state data completion, we compare model performance using mean absolute error (MAE) and root mean square error (RMSE) on the test (missing) data:

$$\text{MAE} = \frac{1}{n} \sum_{i=1}^n |y_i - x_i|,$$

$$\text{RMSE} = \sqrt{\frac{1}{n} \sum_{i=1}^n (y_i - x_i)^2},$$

where n is the number of test samples, and y_i and x_i denote the true and estimated values, respectively.

For (ii) color image inpainting and (iii) color video completion, we use peak signal-to-noise ratio (PSNR) and structural similarity (SSIM) as quantitative metrics. Higher PSNR and SSIM values indicate better recovery quality. For (iv) MRI image completion, we report PSNR, MAE, and RMSE. In the case of video data, PSNR and SSIM are computed per frame and then averaged, while for the MRI data, PSNR is calculated for each frontal slice and the mean value is reported.

A. Traffic Speed Imputation

1) *Datasets*: We evaluate GLSKF on missing data imputation using two publicly available traffic speed datasets under both random and nonrandom missing scenarios with various sampling rates (SR). The datasets are as follows:

- **Seattle Freeway Traffic Speed (S)¹**: This dataset contains traffic speed measurements collected from 323 loop detectors on Seattle highways throughout 2015, with a 5-minute interval (288 time points per day). We use data from 30 consecutive days (January 1st to 30th), organized as a tensor of size $323 \times 288 \times 30$ (location \times time points per day \times day).
- **PeMS-Bay Traffic Speed (P)²**: This dataset contains traffic speed data from 325 loop detectors across the Bay Area, CA. For our experiments, we use a one-month subset (February 1st to 28th, 2017) from 319 detectors, aggregated into a 10-minute time window (144 time points per day). The data is organized as a tensor of size $319 \times 144 \times 28$.

For both datasets, we simulate random missing (RM) scenarios by randomly removing data points at sampling rates of $\{0.7, 0.3, 0.1\}$, corresponding to 30%, 70%, and 90% missing data, respectively.

2) *Configuration: Baselines*. We compare GLSKF with several widely used low-rank completion methods, including:

- **HaLRTC** (High accuracy Low Rank Tensor Completion) [8]: A basic nuclear norm minimization-based tensor completion method.
- **SPC** (Smooth PARAFAC Tensor Completion) [10]: A tensor CP factorization model with total variation (TV) or quadratic variation (QV) smoothness constraints.
- **GRALS** (Graph Regularized Alternating Least Squares) [11]: A low-rank model with graph Laplacian constraints.
- **TRMF** (Temporal Regularized Matrix Factorization) [15]: A matrix factorization model regularized by a temporal autoregressive (AR) process.

In addition, we compare against ablation variants of GLSKF that remove certain constraints:

- **LSTF** (Least Squares Tensor Factorization): A basic tensor factorization model without any smoothness constraints.
- **LSKF** (Least Squares Kernelized Tensor Factorization): A special GLSKF with only the \mathcal{M} component.
- **GLSlocal**: A special GLSKF that estimates only the local component \mathcal{R} with covariance constraints.

Settings. We use the same settings of kernel functions for the two datasets. For the spatial *location* dimension ($d = 1$), we first construct a Laplacian matrix $\mathbf{Lap} \in \mathbb{R}^{I_1 \times I_1}$ using an exponential kernel:

$$k_{\text{exp}}(x_i, x_j; l) = \exp\left(-\frac{\Delta_{ij}}{l^2}\right), \quad (22)$$

where Δ_{ij} denotes the distance between the i th and j th inputs x_i and x_j , which here represents the road network distance between two sensors, and l is considered as a length-scale kernel hyperparameter. \mathbf{Lap} is computed with sensor adjacency matrix in the network, i.e., $\{i = 1, \dots, I_1, j = 1, \dots, I_1\}$. Then

¹<https://github.com/zhiyongc/Seattle-Loop-Data>

²<https://github.com/liyaguang/DCRNN>

we use graph regularized Laplacian (RL) kernel to compute \mathbf{K}_1^u , i.e., $k_1^u = k_{\text{RL}}$:

$$k_{\text{RL}}(x_i, x_j; l, \sigma) = k_{\text{RL}}(\mathbf{Lap}; \sigma) = (\mathbf{I}_{I_1} + \sigma^2 \mathbf{Lap})^{-1}, \quad (23)$$

where l is used to compute the Laplacian matrix. With RL kernel, the inverse of \mathbf{K}_d^u in Eq. (14) can be directly computed with $(\mathbf{I}_{I_1} + \sigma^2 \mathbf{Lap})$. Note that using a graph RL kernel constraint, the problem for the spatial dimension becomes the problem defined in GRALS [11], see Eq. (1). For the local component, we use a tapered RL kernel to compute a sparse banded covariance matrix \mathbf{K}_1^r , i.e., $k_1^r = k_{\text{RL}} k_{\text{taper}}$, where

$$k_{\text{taper}}(x_i, x_j; \lambda) = \begin{cases} \left(1 - \frac{\Delta_{ij}}{\lambda}\right) \cos\left(\pi \frac{\Delta_{ij}}{\lambda}\right) + \frac{1}{\pi} \sin\left(\pi \frac{\Delta_{ij}}{\lambda}\right) & \Delta_{ij} < \lambda \\ 0 & \Delta_{ij} \geq \lambda \end{cases} \quad (24)$$

is set as a Bohman taper [33]. For the second temporal *time of day* dimension ($d = 2$), we use Matérn 3/2 kernel for \mathbf{K}_2^u , that is $k_2^u = k_{\text{Matérn } 3/2}(x_i, x_j; l, \sigma) = \sigma^2 \left(1 + \frac{\sqrt{3}\Delta_{ij}}{l}\right) \exp\left(-\frac{\sqrt{3}\Delta_{ij}}{l}\right)$, and use a tapered Matérn 3/2 kernel to compute \mathbf{K}_2^r , i.e., $k_2^r = k_{\text{Matérn } 3/2} k_{\text{taper}}$, where the tapering function is still Bohman kernel. For the third *day* dimension ($d = 3$), we set both \mathbf{K}_3^u and \mathbf{K}_3^r as the identity matrix \mathbf{I}_{I_3} . We set the variances as 1, i.e., $\sigma = 1$, for all covariance matrices and balance the weights of the regularizers through $\{\rho, \gamma\}$. The length-scale and tapering range hyperparameters $\{l, \lambda\}$ are selected empirically. Specifically, for the Seattle dataset, under all tested scenarios:

- For the first spatial *location* dimension, we set the length-scale $l = 1$ in k_{RL} for \mathbf{K}_1^u , and use $l = 1$ in k_{RL} with tapering range $\lambda = 10$ in k_{taper} for \mathbf{K}_1^r ;
- For the second *time of day* dimension, we set the length-scale for the Matérn kernel to 40 for \mathbf{K}_2^u , and set $l = 5$ with a tapering range of $\lambda = 30$ in k_2^r for \mathbf{K}_2^r .

The kernel hyperparameters for the PeMS dataset are set similarly. These applied kernel hyperparameter values are interpretable and align well with the characteristics of the test datasets.

We set the tensor CP rank $R = 20$ for \mathcal{M} computation in all tested scenarios. For the weight parameters, we select ρ from $\{1, 5, 10, 15, 20\}$ and choose γ from $\{1/10, 1/5, 1, 5, 10\}$ based on the ground truth.

For baselines with structures similar to GLSKF (LSTF, LSKF, GLSlocal), we use the same rank ($R = 20$) and set the covariances and weight parameters ρ and γ as in GLSKF; additionally, the α parameter in LSTF is tuned from $\{0.1, 0.2, 1, 5, 10\}$. In addition, we follow the following specific settings:

- HaLRTC uses a regularization parameter selected from $\{10^{-4}, 10^{-5}\}$.
- SPC is tested with both TV and QV constraints, and the best performance is reported.
- GRALS is implemented with kernelized tensor CP decomposition, where the spatial and time-of-day dimensions are constrained by graph Laplacian covariances (using the same Laplacian as in GLSKF for the spatial

dimension and a first-order adjacency-based Laplacian for the time-of-day dimension), while the day dimension is set to identity.

- In TRMF, the data is reshaped as a matrix (location \times time points), and the temporal lags are set to $\{1, 2, 288\}$ for Seattle and $\{1, 2, 144\}$ for PeMS-Bay.

For baselines with structures similar to GLSKF (LSTF, LSKF, GLSlocal), we use the same rank ($R = 20$) and set the covariances and weight parameters ρ and γ as in GLSKF; additionally, the α parameter in LSTF is tuned from $\{0.1, 0.2, 1, 5, 10\}$.

3) *Results*: Table II presents the imputation performance (MAE and RMSE) for the two datasets under different missing scenarios. Figure 1 displays daily examples of the imputed results for the Seattle dataset under 70% and 90% missing (SR = 0.3 and 0.1, respectively). The results show that GLSKF consistently achieves the lowest estimation errors. Specifically, GLSKF effectively captures both the long-range daily patterns and short-scale local smoothness features, even under a low sampling rate (SR = 0.1). In contrast, HaLRTC produces only basic low-rank reconstructions, while SPC, GRALS, and TRMF capture the global structure but often miss finer details. Among the ablation variants, LSKF yields smoother results than LSTF due to the covariance constraints, and GLSlocal performs comparably to SPC at moderate missing rates but degrades at higher missing rates. Overall, GLSKF outperforms all competing models by effectively leveraging both global low-rank structures and local correlation patterns.

B. Color Image Inpainting

1) *Datasets*: We evaluate GLSKF on color image inpainting, where random pixels are missing at sampling rates (SR) of $\{0.2, 0.1, 0.05\}$ (i.e., 80%, 90%, and 95% missing). We select seven benchmark color images as test data (see Figure 2). The images are represented as third-order tensors with dimensions *columns* \times *rows* \times *channels*; four images have a size of $256 \times 256 \times 3$ and three are $512 \times 512 \times 3$.

2) *Configuration*: **Baselines**. We compare GLSKF with HaLRTC [8], SPC [10], and three related models: LSTF, LSKF, and GLSlocal.

Settings. For the first and second (pixel) dimensions, we use the Matérn 3/2 kernel to compute \mathbf{K}_1^u and \mathbf{K}_2^u , and a tapered Matérn 3/2 kernel with a Bohman taper to obtain \mathbf{K}_1^r and \mathbf{K}_2^r . For the third (channel) dimension, we set $\mathbf{K}_3^u = \mathbf{I}_3$ (i.e., assume independence) and learn \mathbf{K}_3^r as the covariance of the rows of the mode-3 unfolding of \mathcal{R} . In all kernels, the variance is fixed to 1. For the pixel dimensions, we set the length-scale for the latent factor covariances to $l = 30$ and, for the local component, $l = 5$ with a tapering range $\lambda = 30$. We fix the tensor CP rank at $R = 10$ and tune the weight parameters ρ and γ from $\{1, 5, 10, 15, 20\}$ and $\{0.1, 0.2, 1, 5, 10\}$, respectively.

For the baseline methods, HaLRTC is run with a regularization parameter selected from $\{10^{-4}, 10^{-5}\}$. SPC is implemented with TV and QV constraints, and the best results are reported. The baselines LSTF, LSKF, and GLSlocal use the same rank ($R = 10$) and similar covariance configurations as

TABLE II: Comparison of traffic speed imputation (MAE/RMSE).

Data	SR	HaLRTC	SPC	GRALS	TRMF	LSTF	LSKF	GLSlocal	GLSKF
(S) $323 \times 288 \times 30$	0.7	2.42/3.70	2.52/3.70	3.14/5.11	2.87/4.52	3.17/5.13	3.15/5.10	2.28/3.40	2.23/3.35
	0.3	3.13/4.81	2.66/3.98	3.17/5.13	2.95/4.64	3.20/5.18	3.17/5.15	2.78/4.26	2.47/3.80
	0.1	4.29/6.29	2.96/4.54	3.31/5.33	3.44/5.34	3.32/5.36	3.24/5.25	4.16/6.65	2.83/4.49
(P) $319 \times 144 \times 28$	0.7	1.24/2.29	2.07/3.68	2.02/3.76	2.13/3.75	2.04/3.78	2.02/3.75	0.92/1.77	0.86/1.64
	0.3	1.98/3.57	2.18/3.81	2.06/3.81	2.27/4.04	2.10/3.83	2.06/3.79	1.46/2.88	1.19/2.36
	0.1	3.05/4.95	2.53/4.34	2.13/4.31	3.11/5.21	2.41/4.50	2.20/4.07	2.84/5.32	1.78/3.43

Best results are highlighted in bold fonts.

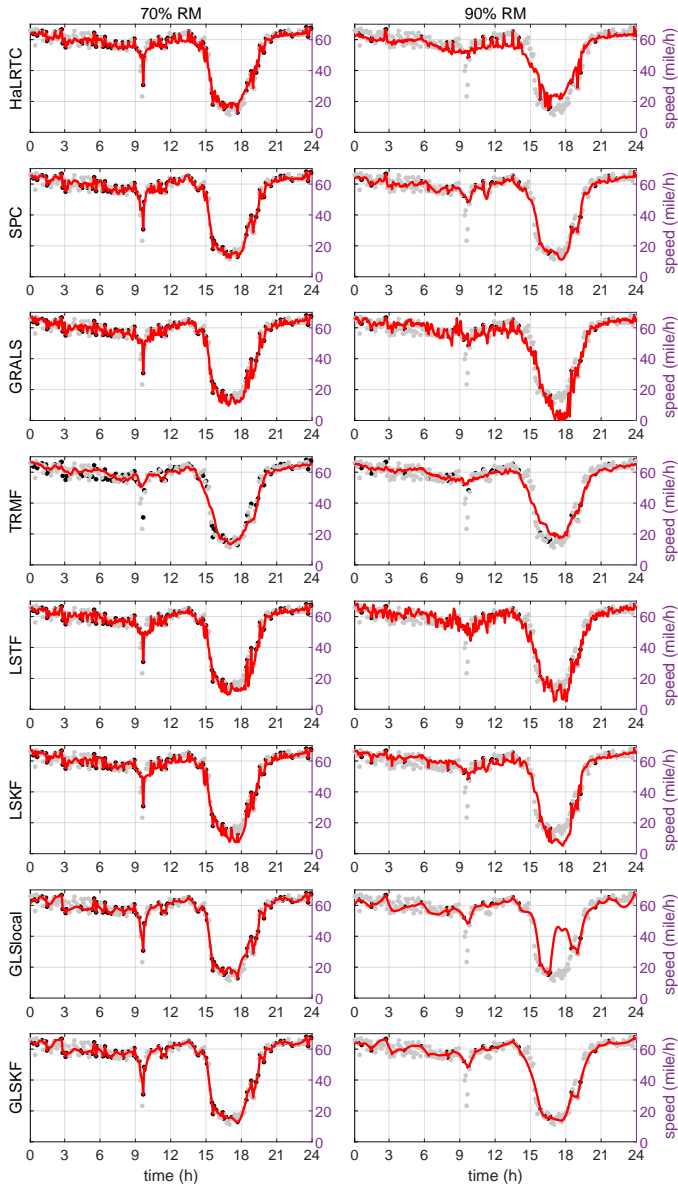


Fig. 1: Illustration of traffic speed imputation, including the imputed results for day 15 at location 200 of (S) data 70% RM (first column) and 90% RM (second column). Black and Grey dots represent the observed and missing data, respectively.

GLSKF; additionally, the α parameter in LSTF is chosen from $\{0.1, 0.2, 1, 5, 10\}$.

3) *Results*: Table III reports the inpainting performance in terms of PSNR and SSIM for the test images under various



Fig. 2: Test color images.

missing rates. Figure 3 shows the completed images under 90% missing. As illustrated, GLSKF consistently delivers the best inpainting results—both quantitatively (with higher PSNR and SSIM) and visually—across nearly all test images. Compared to the purely low-rank methods LSTF and LSKF, which achieve only modest improvements, GLSKF benefits from the complementary integration of global and local components. In particular, LSKF shows some enhancement over LSTF at high missing rates (e.g., 95% RM) due to the incorporation of smoothness constraints, while GLSlocal performs comparably to SPC at lower missing rates but significantly underperforms at higher missing rates because of its lack of a strong low-rank structure. By combining a global low-rank model with a local correlated module, GLSKF achieves superior reconstruction quality even with a small rank ($R = 10$), validating the effectiveness of our complementary model structure.

C. Color Video Completion

1) *Datasets*: We next evaluate GLSKF on a fourth-order color video completion task. We consider three benchmark color video datasets³: *Hall* (H), *Foreman* (F), and *Carphone* (C). Each video is represented as a tensor of size $144 \times 176 \times 3 \times 300$ (height \times width \times channels \times frames). For each video, we randomly remove pixels according to sampling rates (SR) of $\{0.2, 0.1, 0.05\}$, corresponding to 80%, 90%, and 95% missing data.

2) *Configuration*: **Baselines**. We compare GLSKF with HaLRTC [8], SPC [10], and three baseline methods that share similar model structures: LSTF, LSKF, and GLSlocal.

Settings. For the covariance constraints on the latent factors, we use the Matérn 3/2 kernel to compute $\{\mathbf{K}_1^u, \mathbf{K}_2^u, \mathbf{K}_4^u\}$ for the first (pixel), second (pixel), and fourth (frame) dimensions. For the third (channel) dimension, we assume independence by setting $\mathbf{K}_3^u = \mathbf{I}_3$. For the local component, we employ a tapered Matérn 3/2 kernel with a Bohman taper to construct $\{\mathbf{K}_1^r, \mathbf{K}_2^r, \mathbf{K}_4^r\}$. The covariance for the channel dimension, \mathbf{K}_3^r , is computed as the row covariance of the mode-3 unfolding of \mathcal{R} . For the first two dimensions, we set the latent factor

³<http://trace.eas.asu.edu/yuv/>

TABLE III: Comparison of color image inpainting (PSNR/SSIM).

Data	SR	HaLRTC	SPC	LSTF	LSKF	GLSlocal	GLSKF	
Color image $256 \times 256 \times 3$	Barbara	0.2	22.36/0.599	27.01/0.812	21.14/0.531	21.55/0.580	26.26/0.808	27.85/0.857
		0.1	18.58/0.393	24.83/0.730	19.69/0.412	20.70/0.523	23.77/0.717	25.57/0.791
		0.05	15.32/0.249	22.68/0.636	12.77/0.085	19.64/0.452	20.24/0.578	23.36/0.716
	Baboon	0.2	20.17/0.441	22.79/0.621	20.38/0.436	20.79/0.469	22.15/0.597	22.65/0.638
		0.1	17.81/0.289	21.38/0.486	18.22/0.265	19.93/0.364	20.54/0.469	21.11/0.510
		0.05	15.00/0.191	20.31/0.384	13.12/0.083	18.94/0.282	18.26/0.345	20.50/0.421
	House256	0.2	23.98/0.659	27.61/0.803	22.43/0.590	23.21/0.653	27.97/0.817	29.43/0.856
		0.1	20.27/0.471	25.73/0.748	20.97/0.463	22.17/0.588	24.62/0.714	26.97/0.785
		0.05	16.64/0.312	24.03/0.695	15.23/0.145	21.70/0.549	19.49/0.539	25.08/0.739
Peppers	0.2	20.58/0.537	25.85/0.810	19.41/0.463	19.59/0.523	26.65/0.862	27.38/0.864	
	0.1	16.62/0.334	23.60/0.738	17.65/0.316	18.74/0.457	23.61/0.773	24.92/0.798	
	0.05	13.38/0.210	21.55/0.659	11.35/0.071	18.04/0.393	19.70/0.627	22.91/0.735	
Color image $512 \times 512 \times 3$	Sailboat	0.2	22.24/0.761	25.93/0.884	20.28/0.620	20.44/0.639	25.62/0.889	26.77/0.908
		0.1	19.27/0.593	23.79/0.806	19.20/0.526	19.82/0.568	23.07/0.776	24.56/0.847
		0.05	16.74/0.442	21.91/0.707	16.62/0.364	19.35/0.516	19.47/0.578	22.99/0.786
	House512	0.2	23.56/0.802	26.39/0.885	21.30/0.682	21.30/0.688	26.15/0.904	27.52/0.922
		0.1	20.41/0.642	24.30/0.814	20.31/0.594	20.60/0.617	23.25/0.777	24.86/0.867
		0.05	17.91/0.500	22.45/0.724	18.03/0.461	20.05/0.561	19.18/0.540	23.30/0.804
	Airplane	0.2	24.57/0.843	26.54/0.892	21.61/0.709	21.67/0.719	27.76/0.932	30.13/0.959
		0.1	20.92/0.693	24.92/0.843	20.70/0.621	21.24/0.674	23.96/0.790	27.43/0.933
		0.05	18.21/0.552	23.35/0.784	18.18/0.484	20.48/0.603	18.46/0.501	25.03/0.882

Best results are highlighted in bold fonts.

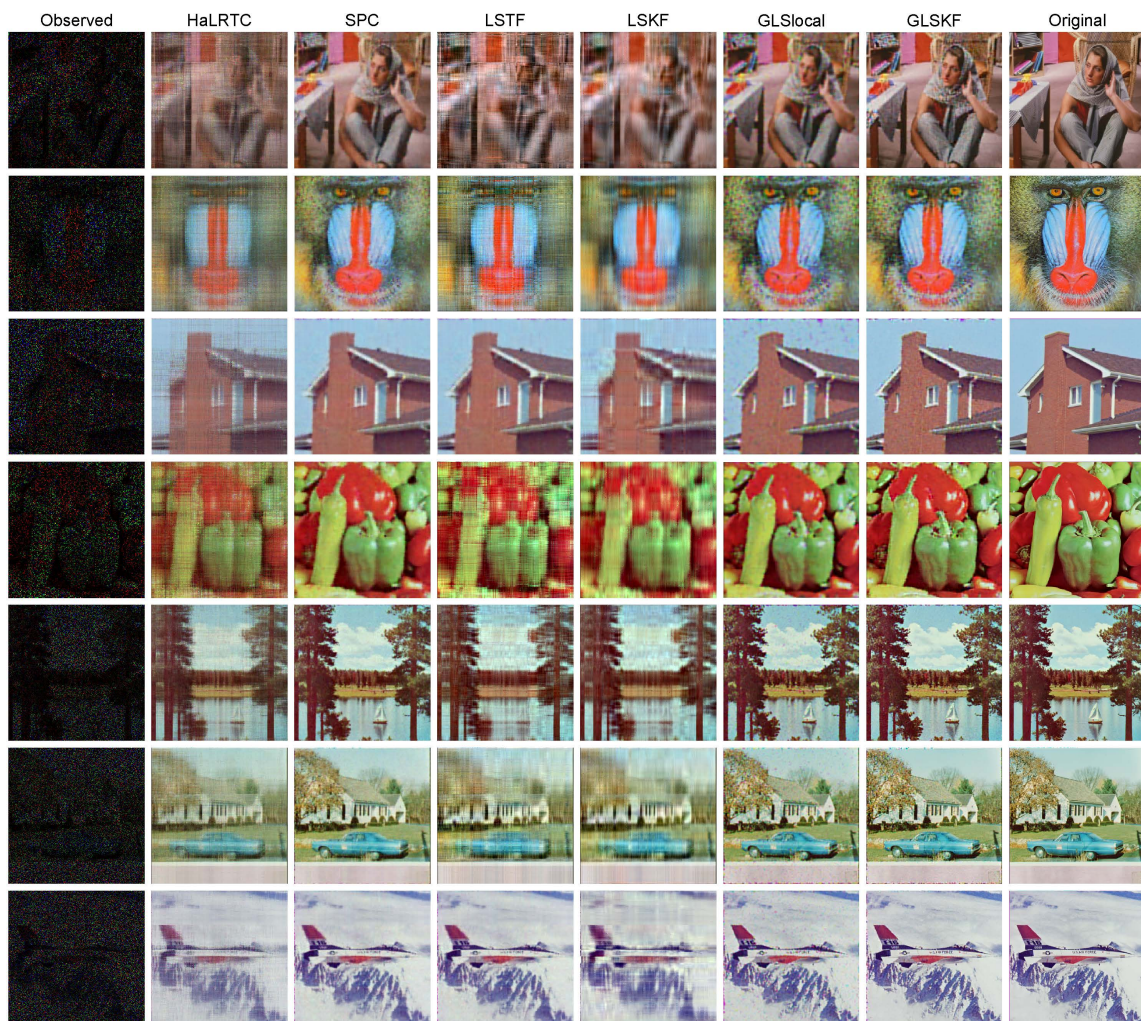


Fig. 3: Results of image inpainting under 90% RM, i.e., SR = 0.1.

TABLE IV: Comparison of color video completion (PSNR/SSIM).

Data	SR	HaLRTC	SPC	LSTF	LSKF	GLSlocal	GLSKF
Hall $144 \times 176 \times 3 \times 300$	0.2	27.41/0.886	30.70/0.924	24.80/0.757	24.60/0.745	30.94/0.945	34.06/0.961
	0.1	23.59/0.786	29.81/0.914	24.25/0.741	23.89/0.730	27.16/0.891	31.74/0.935
	0.05	20.57/0.665	27.97/0.885	23.82/0.733	23.63/0.706	23.93/0.802	29.39/0.900
Foreman $144 \times 176 \times 3 \times 300$	0.2	23.00/0.642	26.31/0.761	20.05/0.488	20.06/0.491	29.26/0.874	32.25/0.920
	0.1	19.69/0.476	24.91/0.705	19.62/0.467	19.43/0.463	26.64/0.801	29.48/0.865
	0.05	17.25/0.390	23.50/0.645	19.30/0.452	18.97/0.449	24.34/0.715	27.34/0.802
Carphone $144 \times 176 \times 3 \times 300$	0.2	25.98/0.807	29.12/0.864	21.87/0.626	21.91/0.625	30.76/0.919	33.01/0.943
	0.1	22.21/0.676	27.63/0.828	21.46/0.609	21.42/0.605	28.11/0.869	30.60/0.903
	0.05	19.21/0.562	27.19/0.818	21.31/0.601	21.23/0.597	25.77/0.805	28.16/0.866

Best results are highlighted in bold fonts.

kernel length-scale to $l = 30$ and the local component kernel length-scale to $l = 5$ with tapering range $\lambda = 10$. For the fourth (frame) dimension, the length-scale is set to 5 for both the latent and local components, with a tapering range of 10. We fix the tensor CP rank at $R = 10$ for global component estimation and select the regularization parameters ρ and γ from $\{0.1, 0.2, 1, 5, 10\}$ based on the ground truth.

For the baseline methods, HaLRTC is run with a regularization parameter chosen from $\{10^{-4}, 10^{-5}\}$, and SPC is implemented using QV-based regularization with smoothness parameters set to $\{0.5, 0.5, 0.5\}$ across the three dimensions. The same rank settings are used for LSTF and LSKF, and the α parameter in LSTF is selected from $\{0.1, 0.2, 1, 5, 10\}$.

3) *Results*: Table IV summarizes the reconstruction performance (PSNR/SSIM) on the three video datasets. Figure 4 presents visual results for the 40th and 220th frames under 80%, 90%, and 95% missing data. Among the baselines, SPC outperforms most methods except GLSlocal (especially on the *Foreman* and *Carphone* datasets), where the temporal continuity helps GLSlocal reconstruct data reasonably even under extreme conditions (e.g., 95% RM). However, GLSKF consistently delivers superior performance across all scenarios, demonstrating the effectiveness of combining global and local components to capture both overall patterns and fine details.

D. MRI Image Completion

1) *Datasets*: We evaluate GLSKF on MRI image completion using a simulated MRI image from BrainWeb⁴. The data is represented as a third-order tensor of size $220 \times 220 \times 184$ (height \times width \times depth). Figure 5 shows eight frontal slices (grayscale images of size 220×220) from the dataset. Following the settings for color image and video completion, we randomly remove 80%, 90%, 95%, and 99% of the entries, corresponding to sampling rates (SR) of $\{0.2, 0.1, 0.05, 0.01\}$.

2) *Configuration*: **Baselines**. We compare the proposed GLSKF framework with HaLRTC [8], SPC [10], and three baselines: LSTF, LSKF, and GLSlocal on the MRI image.

Settings. We employ the Matérn 3/2 kernel to compute $\{\mathbf{K}_1^u, \mathbf{K}_2^u, \mathbf{K}_3^u\}$ for the latent factors and use a tapered Matérn 3/2 kernel (with Bohman taper) to construct $\{\mathbf{K}_1^r, \mathbf{K}_2^r, \mathbf{K}_3^r\}$. For the first two dimensions, the length-scale is set to $l = 30$ and the tapering range to $\lambda = 10$, as used in our color video

experiments. For the third (depth) dimension, we use a shorter length-scale of 5 with a tapering range of 10. The tensor CP rank is fixed at 10, and the weight parameters ρ and γ are selected from $\{0.1, 0.2, 1, 5, 10\}$. For the baseline methods, HaLRTC is run with a regularization parameter of 10^{-2} , and SPC is configured with quadratic variation (QV) regularization using smoothness parameters $\{0.5, 0.5, 0.5\}$ across the three dimensions. The same rank settings are used for LSTF and LSKF, and their other parameters are set similarly to those for color image/video completion.

3) *Results*: Table V reports the overall completion performance in terms of PSNR, MAE, and RMSE for different sampling rates. Figure 6 illustrates the MRI completion results for eight frontal slices under 80%, 90%, and 95% missing rates. As shown, GLSKF consistently achieves the best performance, delivering the highest PSNR and the lowest estimation errors. Notably, GLSKF effectively reconstructs both high-frequency details, such as edges, and the global structure of the image, even under severe missing conditions (up to 99% RM).

VI. DISCUSSION

A. The Roles of Global and Local Components

In GLSKF, the global low-rank component \mathcal{M} and the local correlated residual \mathcal{R} are additively integrated to complement each other and enhance reconstruction quality. The regularization parameters ρ and γ balance the contributions of \mathcal{M} and \mathcal{R} , respectively. Figure 7 illustrates the distinct roles of these components for image inpainting (using *House256*, *Peppers*, and *Airplane* at 90% RM) and video completion (using *Hall* at 80% RM and *Carphone* at 95% RM). As observed, \mathcal{M} captures the background, low-frequency structures, thereby providing a smooth overall approximation, while \mathcal{R} recovers high-frequency details, such as edges, that are essential for preserving image features. This complementary interaction enables GLSKF to achieve high-quality reconstructions.

B. Model Scalability

GLSKF offers a scalable framework for completing real-world multidimensional data. To demonstrate its efficiency, we compare wall-clock time versus mean squared error (MSE) for GLSKF and competing methods on 90% RM color image inpainting for *House256* ($256 \times 256 \times 3$) and 95% RM video completion for *Carphone* ($144 \times 176 \times 3 \times 300$). We use the same convergence criteria for all models. As shown in

⁴<https://zenodo.org/records/8067595>

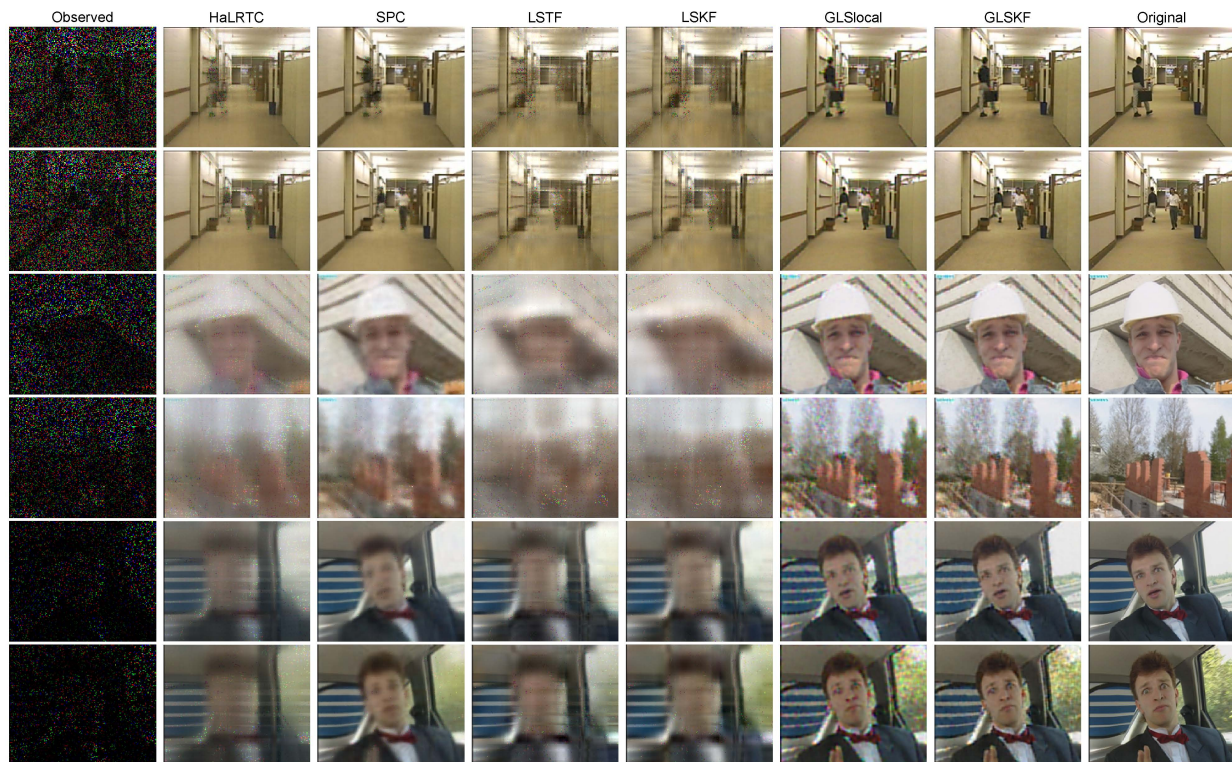


Fig. 4: Illustration of video completion, including the estimated results for the 40th and the 220th frames of the three datasets. Row 1-2, 3-4, and 5-6: reconstruction results for *Hall* 80% RM, *Foreman* 90% RM, and *Carphone* 95% RM, respectively.

TABLE V: Comparison of MRI image completion (PSNR/MAE/RMSE).

SR	HaLRTC	SPC	LSTF	LSKF	GLSlocal	GLSKF
0.2	23.35/0.0396/0.0725	26.55/0.0263/0.0470	21.48/0.0515/0.0882	21.24/0.0514/0.0884	29.04/0.0179/0.0374	29.05/0.0178/0.0371
0.1	20.18/0.0559/0.0963	25.13/0.0289/0.0523	20.74/0.0528/0.0897	20.82/0.0509/0.0886	27.31/0.0207/0.0434	27.34/0.0205/0.0428
0.05	18.07/0.0744/0.1213	23.76/0.0327/0.0592	20.49/0.0529/0.0902	20.36/0.0523/0.0898	25.65/0.0246/0.0513	25.77/0.0238/0.0496
0.01	14.33/0.1248/0.1992	20.29/0.0497/0.0848	18.19/0.0727/0.1203	19.98/0.0537/0.0924	19.80/0.0526/0.1011	22.90/0.0353/0.0685

Best results are highlighted in bold fonts.

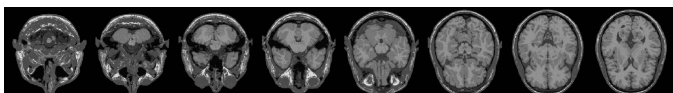


Fig. 5: Eight frontal slices of the test MRI data.

Figure 8, GLSKF initially estimates only the global component, and after K_0 iterations (with $K_0 = 5$ as specified in Algorithm 3) the local component is incorporated. Consequently, the MSE decreases significantly—after approximately 6 seconds for *House256* and 140 seconds for *Carphone*—as the local component begins to contribute to the reconstruction. Compared to other methods, GLSKF demonstrates clear scalability advantages as data size increases, achieving the lowest reconstruction error within a comparable runtime while being significantly more cost-efficient than models such as SPC.

VII. CONCLUSION

In this paper, we proposed the **Generalized Least Squares Kernelized Tensor Factorization (GLSKF)** framework—a complementary low-rank factorization approach for multidimensional data completion. By integrating a generalized least

squares loss into a smoothed low-rank decomposition via covariance norm constraints, GLSKF provides a scalable and elegant model capable of capturing both global, long-range, low-frequency structures and local, high-frequency variations. The framework employs sparse covariance or precision matrices for the local residual component, which, together with projection matrices that preserve the Kronecker structure of the covariances, enables efficient updates through Kronecker matrix-vector multiplications and fast iterative conjugate gradient algorithms. Numerical experiments on four real-world datasets demonstrate that GLSKF outperforms state-of-the-art low-rank methods in both effectiveness and efficiency.

There are several promising directions for future research. For the global low-rank component, the current CP decomposition may be extended to more flexible models, such as Tucker, tensor-ring, or tensor-train decompositions. For the local residual component, alternative techniques—for example, leveraging the Fast Fourier Transform (FFT) for solving linear inverse problems—could be explored, particularly for data on regular grids (e.g., images and videos) where the covariance or precision matrix exhibits a Toeplitz structure. Moreover, the GLSKF framework can be readily adapted to

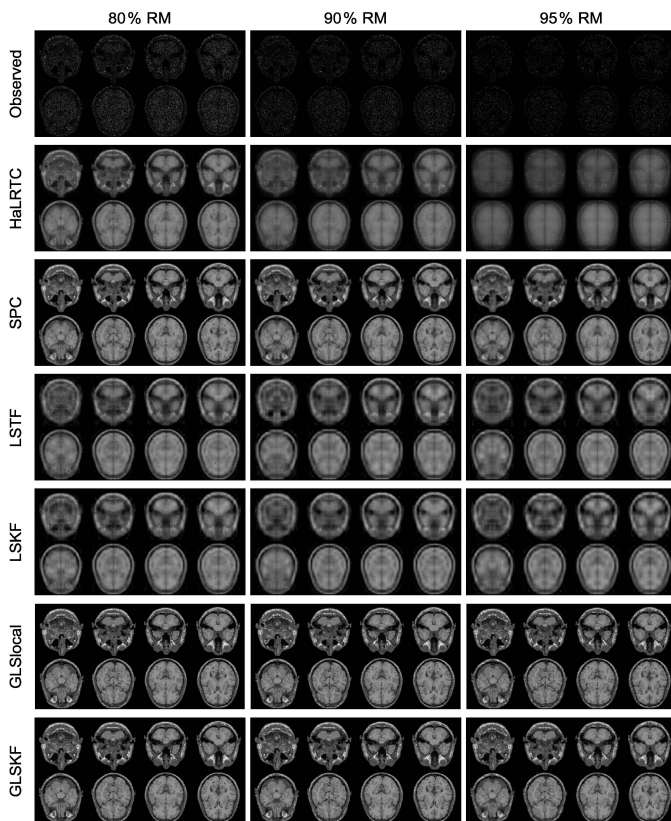


Fig. 6: Illustration results for MRI image completion under three missing rates.

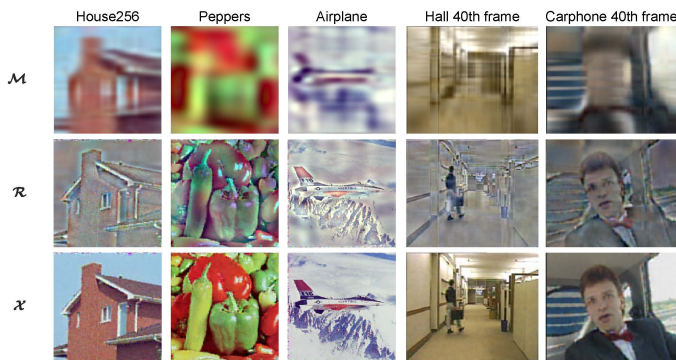


Fig. 7: Visualization of the global component \mathcal{M} , local component \mathcal{R} , and the completed tensor \mathcal{X} . Results are shown for 90% RM color image inpainting on *House256*, *Peppers*, and *Airplane*, as well as for video completion with 80% RM on *Hall* and 95% RM on *Carphone*. For the video data, we show the estimations for the 40th frame. These scenarios correspond to related results in Figures 3 and 4.

related multidimensional data tasks, including denoising and recovery of corrupted data, further broadening its applicability.

ACKNOWLEDGMENTS

This work was supported by the Natural Sciences and Engineering Research Council (NSERC) of Canada Discovery Grant (RGPIN-2019-05950).

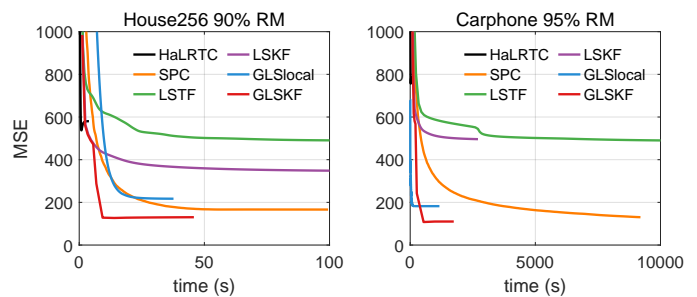


Fig. 8: Comparison of Time vs. MSE for different methods applied to *House256* 90% RM color image inpainting and *Carphone* 95% RM video completion. For *Carphone*, we stop SPC at 2,000 iterations as it shows slow convergence.

REFERENCES

- [1] X. Chen, M. Lei, N. Saunier, and L. Sun, “Low-rank autoregressive tensor completion for spatiotemporal traffic data imputation,” *IEEE Transactions on Intelligent Transportation Systems*, vol. 23, no. 8, pp. 12 301–12 310, 2021.
- [2] M. Lei, A. Labbe, Y. Wu, and L. Sun, “Bayesian kernelized matrix factorization for spatiotemporal traffic data imputation and kriging,” *IEEE Transactions on Intelligent Transportation Systems*, vol. 23, no. 10, pp. 18 962–18 974, 2022.
- [3] H. Chen, M. Lin, J. Liu, H. Yang, C. Zhang, and Z. Xu, “Nt-dptc: a non-negative temporal dimension preserved tensor completion model for missing traffic data imputation,” *Information Sciences*, vol. 653, p. 119797, 2024.
- [4] Y. Panagakis, J. Kossaifi, G. G. Chrysos, J. Oldfield, M. A. Nicolaou, A. Anandkumar, and S. Zafeiriou, “Tensor methods in computer vision and deep learning,” *Proceedings of the IEEE*, vol. 109, no. 5, pp. 863–890, 2021.
- [5] A. Cichocki, D. Mandic, L. De Lathauwer, G. Zhou, Q. Zhao, C. Caiafa, and H. A. Phan, “Tensor decompositions for signal processing applications: From two-way to multiway component analysis,” *IEEE signal processing magazine*, vol. 32, no. 2, pp. 145–163, 2015.
- [6] M. Wang, D. Hong, Z. Han, J. Li, J. Yao, L. Gao, B. Zhang, and J. Chanussot, “Tensor decompositions for hyperspectral data processing in remote sensing: A comprehensive review,” *IEEE Geoscience and Remote Sensing Magazine*, vol. 11, no. 1, pp. 26–72, 2023.
- [7] E. Acar, D. M. Dunlavy, T. G. Kolda, and M. Mørup, “Scalable tensor factorizations for incomplete data,” *Chemometrics and Intelligent Laboratory Systems*, vol. 106, no. 1, pp. 41–56, 2011.
- [8] J. Liu, P. Musialski, P. Wonka, and J. Ye, “Tensor completion for estimating missing values in visual data,” *IEEE transactions on pattern analysis and machine intelligence*, vol. 35, no. 1, pp. 208–220, 2012.
- [9] L. Yuan, C. Li, D. Mandic, J. Cao, and Q. Zhao, “Tensor ring decomposition with rank minimization on latent space: An efficient approach for tensor completion,” in *Proceedings of the AAAI conference on artificial intelligence*, vol. 33, no. 01, 2019, pp. 9151–9158.
- [10] T. Yokota, Q. Zhao, and A. Cichocki, “Smooth parafac decomposition for tensor completion,” *IEEE Transactions on Signal Processing*, vol. 64, no. 20, pp. 5423–5436, 2016.
- [11] N. Rao, H.-F. Yu, P. Ravikumar, and I. S. Dhillon, “Collaborative filtering with graph information: Consistency and scalable methods,” *Advances in Neural Information Processing Systems*, pp. 2107–2115, 2015.
- [12] M. T. Bahadori, Q. R. Yu, and Y. Liu, “Fast multivariate spatio-temporal analysis via low rank tensor learning,” *Advances in Neural Information Processing Systems*, pp. 3491–3499, 2014.
- [13] R. Yu and Y. Liu, “Learning from multiway data: Simple and efficient tensor regression,” *International Conference on Machine Learning*, pp. 373–381, 2016.
- [14] Y. Wang, Y. Zhang, X. Piao, H. Liu, and K. Zhang, “Traffic data reconstruction via adaptive spatial-temporal correlations,” *IEEE Transactions on Intelligent Transportation Systems*, vol. 20, no. 4, pp. 1531–1543, 2018.
- [15] H.-F. Yu, N. Rao, and I. S. Dhillon, “Temporal regularized matrix factorization for high-dimensional time series prediction,” *Advances in neural information processing systems*, vol. 29, 2016.

- [16] L. Xiong, X. Chen, T.-K. Huang, J. Schneider, and J. G. Carbonell, "Temporal collaborative filtering with bayesian probabilistic tensor factorization," in *Proceedings of the 2010 SIAM international conference on data mining*. SIAM, 2010, pp. 211–222.
- [17] M. Lei, A. Labbe, and L. Sun, "Bayesian complementary kernelized learning for multidimensional spatiotemporal data," *arXiv preprint arXiv:2208.09978*, 2022.
- [18] T. Zhou, H. Shan, A. Banerjee, and G. Sapiro, "Kernelized probabilistic matrix factorization: Exploiting graphs and side information," in *Proceedings of the 2012 SIAM international Conference on Data mining*. SIAM, 2012, pp. 403–414.
- [19] M. Lei, A. Labbe, and L. Sun, "Scalable spatiotemporally varying coefficient modeling with bayesian kernelized tensor regression," *Bayesian Analysis*, vol. 1, no. 1, pp. 1–29, 2024.
- [20] G. I. Allen, L. Grosenick, and J. Taylor, "A generalized least-square matrix decomposition," *Journal of the American Statistical Association*, vol. 109, no. 505, pp. 145–159, 2014.
- [21] B. W. Larsen, T. G. Kolda, A. R. Zhang, and A. H. Williams, "Tensor decomposition meets rkhs: Efficient algorithms for smooth and misaligned data," *arXiv preprint arXiv:2408.05677*, 2024.
- [22] C. KI Williams and C. E. Rasmussen, *Gaussian processes for machine learning*. MIT press Cambridge, MA, 2006.
- [23] H. Sang and J. Z. Huang, "A full scale approximation of covariance functions for large spatial data sets," *Journal of the Royal Statistical Society: Series B (Statistical Methodology)*, vol. 74, no. 1, pp. 111–132, 2012.
- [24] M. Katzfuss, "Bayesian nonstationary spatial modeling for very large datasets," *Environmetrics*, vol. 24, no. 3, pp. 189–200, 2013.
- [25] M.-H. Descary and V. M. Panaretos, "Functional data analysis by matrix completion," *The Annals of Statistics*, vol. 47, no. 1, pp. 1–38, 2019.
- [26] T. Masak and V. M. Panaretos, "Random surface covariance estimation by shifted partial tracing," *Journal of the American Statistical Association*, pp. 1–13, 2022.
- [27] X.-L. Zhao, J.-H. Yang, T.-H. Ma, T.-X. Jiang, M. K. Ng, and T.-Z. Huang, "Tensor completion via complementary global, local, and nonlocal priors," *IEEE Transactions on Image Processing*, vol. 31, pp. 984–999, 2021.
- [28] T. G. Kolda and B. W. Bader, "Tensor decompositions and applications," *SIAM Review*, vol. 51, no. 3, pp. 455–500, 2009.
- [29] R. Furrer, M. G. Genton, and D. Nychka, "Covariance tapering for interpolation of large spatial datasets," *Journal of Computational and Graphical Statistics*, vol. 15, no. 3, pp. 502–523, 2006.
- [30] C. G. Kaufman, M. J. Schervish, and D. W. Nychka, "Covariance tapering for likelihood-based estimation in large spatial data sets," *Journal of the American Statistical Association*, vol. 103, no. 484, pp. 1545–1555, 2008.
- [31] H. Rue and L. Held, *Gaussian Markov random fields: theory and applications*. Chapman and Hall/CRC, 2005.
- [32] A. G. Wilson, C. Dann, and H. Nickisch, "Thoughts on massively scalable gaussian processes," *arXiv preprint arXiv:1511.01870*, 2015.
- [33] T. Gneiting, "Compactly supported correlation functions," *Journal of Multivariate Analysis*, vol. 83, no. 2, pp. 493–508, 2002.

Mengying Lei received the M.S. degree from the School of Automation Science and Electrical Engineering, Beihang University, Beijing, China, in 2019, and the Ph.D. degree in Transportation from McGill University, in 2024. She is now a postdoctoral researcher at McGill University, Montreal, Quebec, Canada. Her research currently focuses on spatiotemporal data modeling and intelligent transportation systems.

Lijun Sun (Senior Member, IEEE) received the B.S. degree in Civil Engineering from Tsinghua University, Beijing, China, in 2011, and Ph.D. degree in Civil Engineering (Transportation) from the National University of Singapore in 2015. He is an Associate Professor and William Dawson Scholar with the Department of Civil Engineering at McGill University, Montreal, QC, Canada. His research centers on intelligent transportation systems, machine learning, spatiotemporal modeling, travel behavior, and agent-based simulation.